Chemie der Erde 77 (2017) 399–419

Contents lists available at ScienceDirect

Chemie der Erde

journal homepage: www.elsevier.de/chemer

Mineral geochemistry of the Sangan skarn deposit, NE Iran: Implication for the evolution of hydrothermal fluid

Fatemeh Sepidbar[a,b], Hassan Mirnejad[a,c,*], Jian-Wei Li[b], Chunjing Wei[d], Luke L. George[e], Kingsley Burlinson[f]

[a] Department of Geology, Faculty of Sciences, University of Tehran, Tehran 14155-64155, Iran
[b] State Key Laboratory of Geological Processes and Mineral Resources, China University of Geosciences, Wuhan 430047, People's Republic of China
[c] Department of Geology and Environmental Earth Sciences, Miami University, OH 45056, USA
[d] State Key Laboratory of Orogenic Belts and Crustal Evolution, Peking University, Beijing 100871, People's Republic of China
[e] School of Physical Science, University of Adelaide, Adelaide, SA 5005, Australia
[f] Burlinson Geochemical Services Pty. Ltd., Darwin, NT, Australia

ARTICLE INFO

Article history:
Received 18 April 2017
Received in revised form 5 July 2017
Accepted 14 July 2017
Editorial handling - T. Tomas Magna

Keywords:
Garnet
Clinopyroxene
Magnetite
Iron skarn deposit
Sangan
Iran

ABSTRACT

The Sangan iron skarn deposit is located in the Sabzevar-Dorouneh Magmatic Belt of northeastern Iran. The skarn contains zoned garnet, clinopyroxene and magnetite. Cores and rims of zoned garnets are generally homogeneous, having a relatively high ΣREE, low ΣLREE/ΣHREE ratios, and positive Eu anomalies. The cores of the zoned clinopyroxenes are exceptionally HREE-rich, with relatively high ΣREE and HREE/LREE ratios, as well as positive Eu anomalies. Clinopyroxene rims are LREE-rich, with relatively low ΣREE contents and HREE/LREE ratios, and do not have Eu anomalies. Magnetite grains are enriched in LREEs in comparison with the HREEs and lack Eu anomalies. Variations of fluid composition and physicochemical conditions rather than YAG-type substitution mechanism are considered to have major control on incorporating trace elements, including REE, into the skarn mineral assemblage. Based on baro-acoustic decrepitation analysis, the calc-silicate and magnetite dominant stages were formed at similar temperatures, around 350–400 °C. In the Sangan skarns, hydrothermal fluids shifted from near-neutral pH, reduced conditions with relatively high ΣREE, low LREE/HREE ratios, and U-rich characteristics towards acidic, oxidized conditions with relatively low ΣREE, high LREE/HREE ratios, and U-poor characteristics.

1. Introduction

Skarn deposits are genetically closely related to magmatic intrusions. They form as hydrothermal fluids released at the end of magmatic crystallization and interact with carbonate country rocks through metasomatism (Meinert and Nicolescu, 2005). Mineral assemblages often vary between different skarn zones, but garnet, clinopyroxene, and magnetite are normally the most common and widespread minerals in skarns (*e.g.*, Jamtveit et al., 1993; Somarin, 2004; Ciobanu and Cook, 2004; Chang and Meinert, 2004; Dziggel et al., 2009; Ismail et al., 2014; Zhao and Zhou, 2015; Xu et al., 2016). Garnets from plutonic rocks are generally Fe-rich and exhibit a weak increase in Mn content from core to rim (*e.g.* Mirnejad et al., 2008; Samadi et al., 2014; Ismail et al., 2014; Xu et al., 2016), whereas garnets originating from skarns are often characterized by Al-rich cores and Fe^{3+}-rich rims (Gaspar et al., 2008). Trace elements in skarn minerals are useful geochemical tracers (Cheng et al., 2012; Schmidt et al., 2011). For example, magnetite from genetically different types of deposit displays various trace element patterns depending on fluid/water/melt compositions and processes of magnetite precipitation (*e.g.*, Frietsch and Perdahl, 1995; Dare et al., 2014). Thus magnetite composition may reveal the physicochemical conditions under which it was formed. During contact metamorphism and hydrothermal alteration of carbonate-bearing rocks, garnet and pyroxene grow under a variety of physicochemical conditions (Fernando et al., 2003; Kim, 2006; Martin et al., 2011). These minerals commonly display complex chemical zoning patterns that may record the physicochemical evolution of the hydrothermal system. Chemical composition of garnet and pyroxene has been used to solve various geological problems including understanding the physicochemical condi-

* Corresponding author at: Department of Geology, Faculty of Sciences, University of Tehran, Tehran 14155-64155, Iran.
E-mail address: hmirnejad@ut.ac.ir (H. Mirnejad).

http://dx.doi.org/10.1016/j.chemer.2017.07.008
0009-2819/

tions of formation of both skarn minerals and rocks (Chakraborty and Ganguly, 1991); fO_2 changes in skarn (Kim, 2006), recording regional metamorphic history (Whitney, 1996) and reflecting hydrothermal skarn fluid evolution (Gaspar et al., 2008; Smith et al., 2004; Somarin, 2004; Ismail et al., 2014; Xu et al., 2016). Fluid inclusion studies are mainly carried out on transparent minerals, despite the fact that economic minerals of interest are usually opaque. To understand the fluid conditions during deposition of these deposits it is necessary to study opaque minerals. However, it is difficult but there are three methods to study inclusions in opaque minerals as the baro-acoustic decrepitation method, microscope observations using infrared light, or mass spectrometric analyses of gases released during decrepitation of the sample (Burlinson, 1984, 2012). Magnetite is not transparent under IR, so the baro-acoustic decrepitation method was used to study the fluids in this opaque mineral as well as garnet grains as transparent mineral. In addition to estimating the formation temperature of the opaque minerals, baro-acoustic decrepitation detects the presence of CO_2 rich fluids.

The Sangan iron skarn deposit, northeastern Iran (having a proven reserve of over 1000 Mt iron ore @ 53% Fe, Sangan represents a world-class iron skarn deposit), is located at the eastern edge of the Sabzevar-Dorouneh magmatic belt (SDMB) in the Sangan Magmatic Complex (SMC) (Fig. 1a). The skarn and the iron orebodies defined by surface mapping and diamond drilling extend over 8 km along an E-W trending zone and occur at depths down to 600 m below the surface (Golmohammadi et al., 2015). Previous studies were mainly limited to the alteration and mineralization characteristics of selected parts of the Sangan deposit (Karimpour, 2004; Golmohammadi et al., 2015), thus the fluid evolution of the deposit and chemical compositions of garnet, pyroxene and magnetite, remains incompletely understood. In this study, we report new textural characteristics, systematic major, trace and rare earth element (REE) contents of garnet, pyroxene and magnetite and fluid inclusion studies in garnet and magnetite from the Sangan iron skarn deposit. Data were obtained by electron microprobe (EMPA), *in-situ* laser ablation inductively coupled plasma-mass spectroscopy (LA-ICP-MS), and baro-acoustic decrepitation. The aim of this study was to decipher the fluid evolution responsible for crystallizing garnet, pyroxene and magnetite in Sangan skarn.

2. Geological setting

The oldest unit in the Sangan area is a thick pile (~1500 m) of sedimentary rocks, consisting of Lower Jurassic shale and siltstone, overlain by Upper Jurassic to Cretaceous limestone and dolomite (Kermani and Forster, 1991) (Fig. 1b). This sedimentary sequence is intruded by granitoid intrusions or is unconformably covered by volcanic rocks (Fig. 1b). Granitoids are extensively present in the north of the Sangan area and exhibit a weak alteration consisting of sericite and chlorite. They are pinkish grey and display medium to coarse-grained granular and porphyritic textures. Published zircon U-Pb ages of the Sangan intrusions range from 42 to 38 Ma (Golmohammadi et al., 2015). At the contact between granitoids and carbonate rocks, there is a thermal metamorphic aureole containing iron skarn mineralization (Golmohammadi et al., 2015) (Fig. 1b).

The calc-silicate-dominant stage at Sangan is characterized by replacement of limestone by andradite garnet, hedenbergite, plagioclase and lesser epidote, and rare biotite. The magnetite-dominant stage overprints calc-silicate-dominant stage minerals and produced amphibole, calcite, chlorite, phlogopite, magnetite and sulfides. Iron mineralization and associated skarn at Sangan consists of seven orebodies from west to east (Fig. 1a): A', A, B, C-South (Cs), C-North (Cn), Baghak (BA), and Dardvey (D). Two garnet zones, namely the garnet skarn and the garnet-clinopyroxene skarn zones, formed during the calc-silicate dominant stage. Garnet skarn zones are abundant in the northern part in the areas A', A, Cn, Cs and D (Fig. 1). Field observations indicate that the large magnetite bodies, commonly associated with these skarns, are located along faults or fracture zones. In the Cn skarn, garnet is well represented, forming a zone up to 30 m wide, while the garnet-pyroxene skarn forms a narrow zone, only a few cm wide, similar to the garnet-clinopyroxene zone in D skarn. The contact between the granite and garnet skarn, where observed, is sharp and garnet skarn generally grades outwards into garnet-clinopyroxene skarn. Associated magnetite bodies from the magnetite dominant stage are present in orebodies A, B, Cn and Cs.

3. Analytical methods

3.1. Major-oxide element chemistry

Ten representative samples from orebodies A, A', B, Cn, Cs and D were chosen to investigate the origin and evolution of hydrothermal zoned garnet, pyroxene and magnetite in the deposit. Following detailed textural and petrographic studies, twenty-two polished sections of representative garnet, pyroxene and magnetite were selected for systematic major and trace element analyses. Electron microprobe analysis (EMPA) was performed to acquire compositional data. Mineral compositions were determined at the State Key Laboratory of Geological Processes and Mineral Resources (GPMR), China University of Geosciences (CUG), Wuhan, using a JEOL JXA-8100 EMPA Analyzer equipped with a wavelength-dispersive spectrometer (WDS). Analytical conditions were: an accelerating voltage of 15 kV, a beam current of 20 nA and a 2 μm focused electron beam. Natural and synthetic mineral standards were used for calibration, and matrix correction was done using the ZAF method to convert maps of X-ray intensity data into two-dimensional maps of oxide wt% and cation proportions for the eight major rock-forming elements. Element peaks and backgrounds were measured for all elements with counting times of 10 s and 5 s (except for Ti and Mn, for which count times were 20 s and 10 s, respectively). The accuracy of the reported analytical values is 1–5% relative depending on the element abundance.

3.2. Trace and rare earth element chemistry

Trace element analysis of garnet, pyroxene and magnetite was conducted at the Key Laboratory of Orogenic Belts and Crustal Evolution, Peking University, using an Agilent 7500c ICP-MS system connected with a 193 nm ArF Excimer laser system (COMPexPro 102) with automatic positioning system. Ablation spot size was 60 μm with a repetition rate of 5 Hz and laser energy of 100 mJ. Helium was used as the cell gas. The acquisition times for the background and the ablation interval were 15–20 s and 45–60 s, respectively. Synthetic glasses NIST 610, 612, and 614 were used as external standards. The calculation of trace element concentrations was performed by GLITTER version 4.4.2. The accuracy of the reported analytical values is less than 5% relative depending on the abundance of the element.

3.3. Baro-acoustic decrepitation of fluid inclusions

Baro-acoustic decrepitation analysis was performed to determine the fluid composition and formation temperature of trapped fluid in two magnetite samples (B-4 and C-4) from high-grade massive magnetite ores from B and C orebodies and in one garnet (A-1) hand sample of garnetite from A orebody at the laboratory of Burlinson Geochemical Services Pty. Ltd. in Darwin, Australia. The analyses were done on 0.5 g of sample. There was minor carbonate and sulfide in B-4 and C-4, respectively. Sample B-4 was

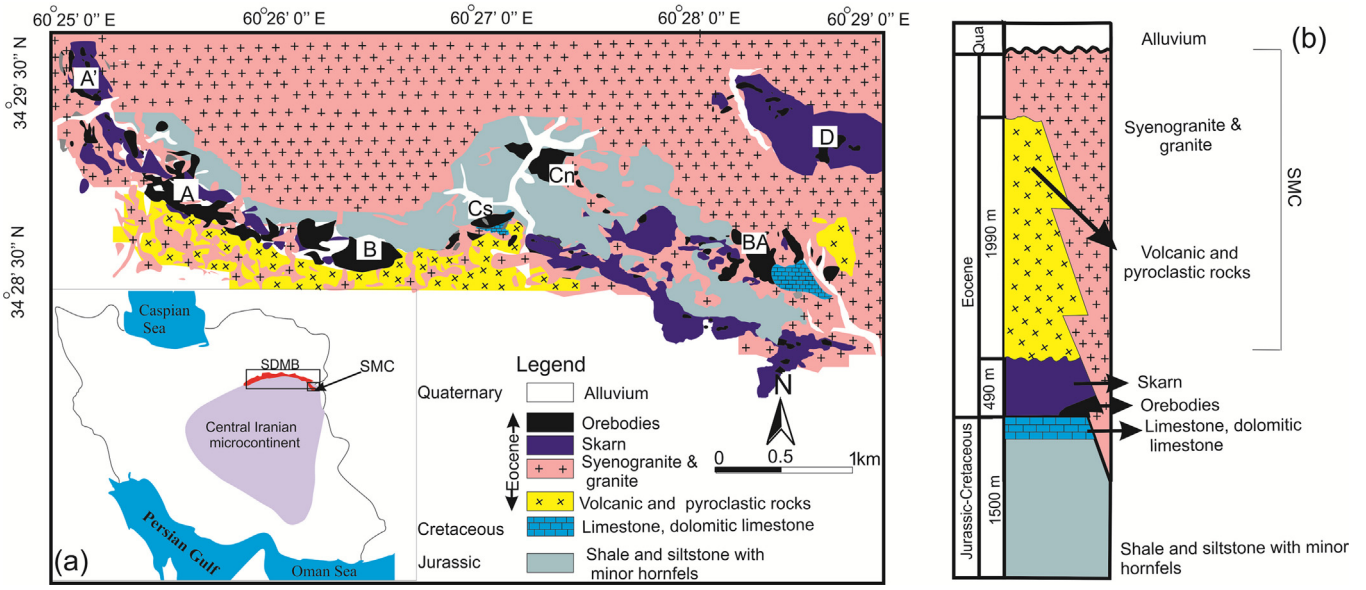

Fig. 1. (a) Map of Iran and geological map of the Sangan region including location of the Sangan deposit and the Eocene plutonic and volcanic rocks based on 1:250,000 geological maps of Taybad (Alavi Naini, 1982). Locations of A, A', Cn, Cs, D and Ba skarn types are shown; (b) Stratigraphic columnar section of the Sangan area (modified after Mazaheri, 1996).

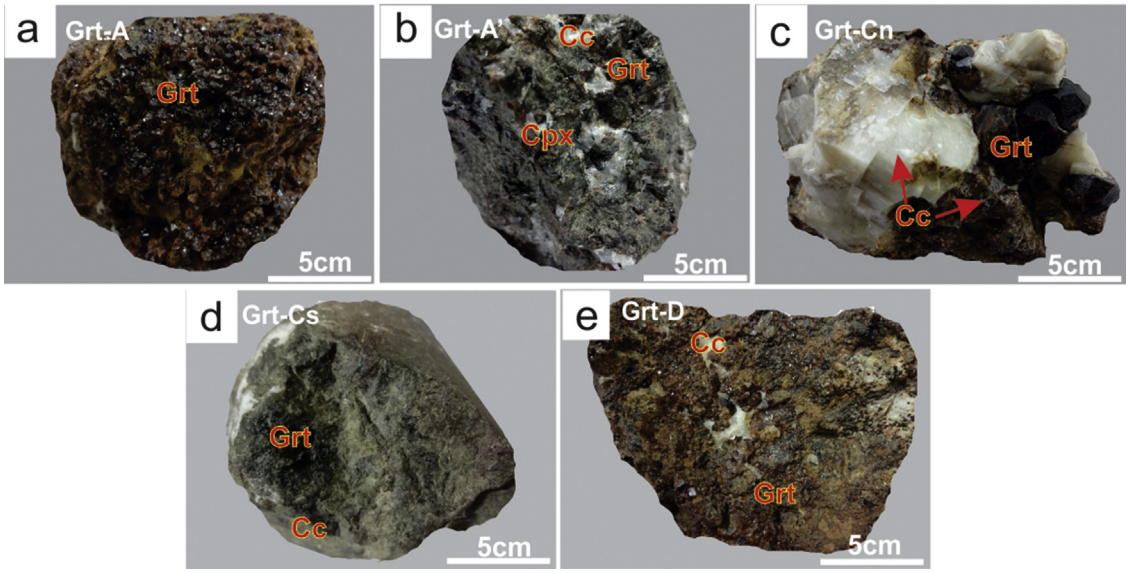

Fig. 2. Representative hand specimens of garnets from different types of Sangan Fe skarn. (a) Red to brown, fine-grained euhedral garnet crystals from A skarn; (b) Green to gray, fine-grained subhedral garnet crystals from A' skarn; (c) Coarse dodecahedral garnet grains of red to brown color from Cn skarn that is replaced by calcite; (d) Fine-grained garnet and associated calcite from Cs skarn; (e) Fine to medium grained brown-colored garnet grains from D skarn. (For interpretation of the references to color in this figure legend, the reader is referred to the web version of this article.)

washed with 10% HCl to remove carbonate while the sulfide in sample C-4 was separated magnetically and by hand. After preparation, magnetite sample B-4 consisted of >95% magnetite/haematite and was weakly magnetic, while magnetite sample C-4 contained rare pyrite grains. Most sulfide was eliminated during magnetic separation, but minor mineral contamination remained. Prior to analysis the sample was crushed and sieved into a fine fraction of 200–420 μm (80–40 mesh). The prepared samples were analyzed with the BGS model 105 decrepitometer (Burlinson, 1990). The samples were heated at 20 °C per minute over a range of 100–800 °C and fluid inclusion bursts were simultaneously recorded digitally (Burlinson, 1988). The decrepitometer was calibrated for quality control of the results using standard samples. Decrepigrams were plotted using Gnuplot, version 4.6 (http://www.gnuplot.info). The ore formation temperature was estimated based on the "onset temperature" (temperature at the toe of the peak), which marks the start of massive decrepitation of fluid inclusions.

4. Petrography

The Sangan deposit is a calcic and magnesian type skarn formed due to the interaction of magmatically-derived hydrothermal fluids and two different protoliths; limestone in the west, and dolostone in the east (Mazaheri, 1996). The calcic skarn in the western zone contains andradite (And)-grossular (Gro)-rich garnet, Ca-Fe-rich pyroxene, ferrohastingsite associated with wollastonite, plagioclase, and K-feldspars in the endoskarns, and ferroactinolite, Fe-rich chlorite, clinochlore, calcite, and magnetite in the

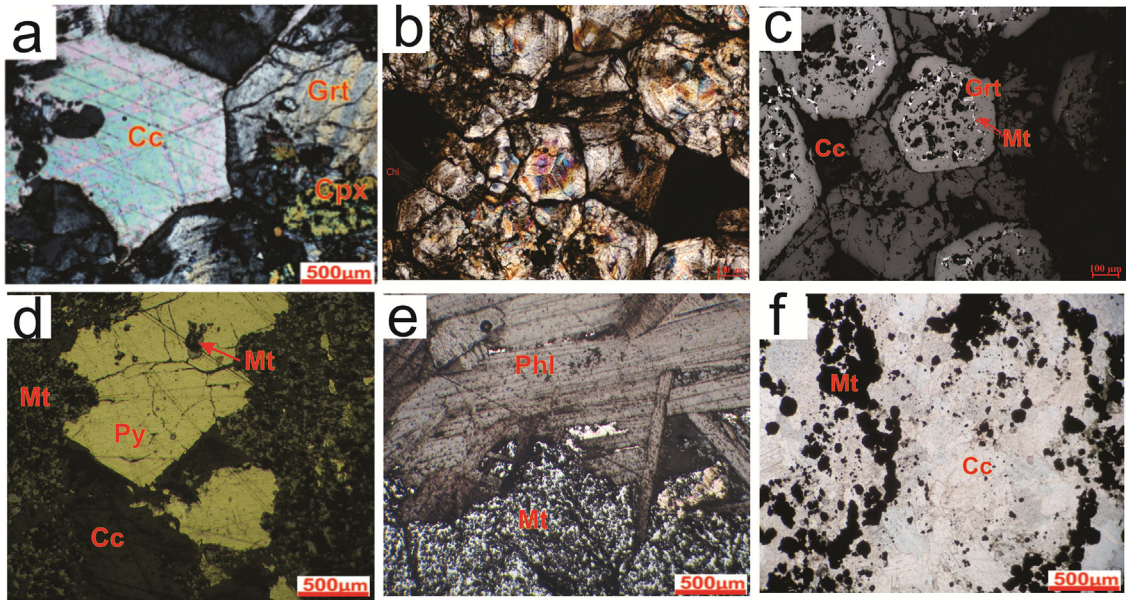

Fig. 3. Representative optical characteristics of garnets from different types of Sangan Fe skarn. (a) Photomicrographs of garnet from A skarn under crossed polarized light = XPL; (b) Dodecahedral garnet and polysynthetic twinning texture in garnet from A' skarn; (c) fracture filled with calcite in garnet from Cn skarn; (d) massive magnetit grains and associated pyrite from calcic skarn; (e) massive magnetite and associated phlogopite in magnesian skarn; (f) Magnetite occurs as disseminated in calcite grains. skarn;. Grt = garnet; Cc = calcite; Mt = magnetite; Phl = phlogopite; Py = pyrite; Cpx = clinopyroxene.

exoskarns. The magnesian skarn in the eastern zone contains forsterite, diopsidic pyroxene, phlogopite, actinolite, serpentine, Mg-chlorite clinochlore, talc, and magnetite (Golmohammadi et al., 2015). Garnet is the predominant mineral in both skarn zones (garnet and garnet-clinopyroxene skarns) in the Sangan deposit. Small (0.5–1 cm) euhedral garnet crystals are very common in all skarns (Fig. 2a–d) while medium to large (1–2 cm) euhedral garnet crystals are located in Cn orebody (Fig. 2e). Garnet-clinopyroxene skarn, cropping out as greenish brown medium to fine-grained (0.10–0.25 cm) rocks, is dominant in the A' skarn (Fig. 2b).

Large garnet grains from Cn often exhibit replacement by calcite (Fig. 2c). The garnet skarns typically preserve granoblastic textures consisting of zoned garnet with minor and variable amounts of calcite, quartz, biotite, amphibole, chlorite, magnetite, and sulfides. Due to physical and chemical condition variations, purity and perfection of garnet crystals during growth conditions (Hariya and Kimura, 1978), this mineral is weakly anisotropic (Fig. 3). Magnetite, the most abundant oxide mineral associated with the garnet skarn, commonly occurs as medium to large grains (Fig. 3a), although magnetite inclusions within garnet are common. The magnetite grains are anhedral to subhedral (20–300 μm) and are enclosed by pyrite in some locations.

Garnet-clinopyroxene skarns typically contain garnet, clinopyroxene, calcite and quartz, together with K-feldspar ± plagioclase and magnetite. Generally, clinopyroxenes form fine-grained (0.1–0.2 cm) anhedral crystals or disseminated grains along garnet grain boundaries. Subhedral to euhedral, pale green clinopyroxene (0.1–0.2 cm), in addition to occurring as inclusions in garnet grains, forms large granoblastic or granular intergrowths with garnet (Fig. 3b). Garnets are normally fresh, but in some places are partly replaced by an assemblage consisting of calcite, quartz and magnetite ± chlorite. Magnetite occurs as inclusions in garnet crystals which are commonly 1 mm in size and are euhedral to anhedral (Fig. 3c). Magnetite is also the most abundant oxide mineral associated with the magnetite-dominant stage and occurs as massive (Fig. 3d and e), disseminated (Fig. 3f), and brecciated ores in the skarn at Sangan. It is found together with minor hematite, pyrite, and calcite (Fig. 3d) in the calcic skarn and with phlogopite (Fig. 3e) in the magnesian skarn. The massive ore shows fine- to medium-grained (up to 2.5 cm in diameter), granoblastic and massive textures (Fig. 3e).

5. Results

5.1. Major element compositions of mineral

Chemical compositions and formulae of garnet grains from Sangan skarn types are reported in Table 1. Garnet compositions are predominantly andradite-grossularite (And-Gro) (grandite) solid solution, rich in Fe and Al, with spessartine component (Spe) less than 5 mol% (Fig. 4). Garnet from A skarn displays wide variations in contents of andradite (And; 50.6–76.3%), grossular (Gro; 22.1–47.3%), pyrope (Pyr; up to 0.4%), almandine (Alm; up to 0.9%) and spessartine (Spe; 1.3–1.9%, Table 1). Garnet from A' has less And content (40.8–55.4%), and more Gro content (39.7–55.2%) than that of garnet from A skarn. Garnet from D skarn also shows wide variation in And (57.3–74.0%), Gro (24.7–40.5%), Pyr (up to 0.5%) and Alm (up to 0.8%) contents, as does garnet from Cn (And; 48.9–68.3%, Gro; 29.8–48.1%, Pyr; up to 0.4%, Alm; up to 1.6% and Spe; 1.4–2.5%). Garnet from Cs skarn shows narrow variations in contents of And (50.9–60.9%), Gro (36.9–46.3%), Pyr (up to 0.15%), Alm (0.21–1.13%) and Spe (1.43–1.60%).

Garnets with Al-rich cores and Fe-rich rims are common in skarn system; however homogeneous garnets and garnets with Fe-rich cores and Al-rich rims may also exist (Meinert, 1992, 1997). Within the Sangan skarns, some garnet crystals show subtle Fe^{+3} enrichment in rims relative to cores (Fig. 5). In general, garnetite samples from different orebodies are intermediate grandites (Fig. 4) and anisotropic (Fig. 3a and b). Garnets of the A, A' and Cn orebodies formed by epitaxial growth with zoning and have trapezohedral faces (Fig. 5a, d and g). These garnet grains show Fe-enriched and Al-depleted rims rather than cores (Fig. 5b, c, e, f h, i). Garnet grains from Cs and D also show zoning (Fig. 5d, m) with intense fractures (Fig. 5j), but are not Fe-enriched and Al-depleted from rim to core

Table 1
(a) Selected electron microprobe analyses of garnet from A orebody. (b) Selected electron microprobe analyses of garnet from A' orebody. (c) Selected electron microprobe analyses of garnet from D orebody. (d) Selected electron microprobe analyses of garnet from Cn orebody. (e) Selected electron microprobe analyses of garnet from Cs orebody.

(a)

Sample	Grt-A-011 core	Grt-A-04 core	Grt-A -05 core	Grt-A -06 core	Grt-A -07 core	Grt-A -08 rim	Grt-A -09 rim	Grt-A -010 rim
SiO_2	37.98	37.74	37.44	38.02	37.96	37.79	37.03	37.24
TiO_2	0.348	0.251	0.163	0.29	0.41	0.051	0.109	0.017
Al_2O_3	10.78	9.320	8.200	10.35	10.79	5.750	4.320	6.430
FeO	15.64	17.43	18.62	16.26	15.95	22.24	23.35	21.55
MnO	0.860	0.760	0.680	0.750	0.900	0.720	0.574	0.580
MgO	0.080	0.100	0.060	0.072	0.042	0.000	0.091	0.030
CaO	35.14	35.23	35.29	34.73	34.95	35.23	35.25	35.01
Number of cations on the basis of 12 oxygens								
Si	2.967	2.965	2.966	2.982	2.963	2.982	2.972	2.962
Ti	0.020	0.015	0.010	0.017	0.024	0.003	0.006	0.001
Al	0.992	0.862	0.765	0.957	0.992	0.534	0.408	0.602
Cr	0.000	0.000	0.000	0.000	0.000	0.000	0.000	0.000
Fe^{3+}	1.016	1.145	1.234	1.044	1.016	1.468	1.567	1.422
Fe^{2+}	0.005	0.000	0.000	0.023	0.025	0.000	0.000	0.011
Mn	0.057	0.051	0.046	0.050	0.059	0.048	0.039	0.039
Mg	0.009	0.012	0.007	0.008	0.005	0.000	0.011	0.003
Ca	2.941	2.966	2.996	2.919	2.923	2.979	3.031	2.983
Ura	0.000	0.000	0.00	0.000	0.000	0.000	0.000	0.000
Pyr	0.310	0.390	0.23	0.280	0.160	0.000	0.350	0.120
Spe	1.880	1.670	1.50	1.660	1.980	1.580	1.270	1.290
Gro	47.03	41.22	37.57	45.11	46.44	25.68	22.10	27.98
And	50.60	56.72	60.69	52.17	50.58	72.74	76.28	70.24
Alm	0.180	0.000	0.000	0.780	0.840	0.000	0.000	0.370

(b)

Sample	Grt-A'-011 rim	Grt-A'-012 rim	Grt-A'-013 rim	Grt-A'-014 core	Grt-A'-015 core	Grt-A'-016 core	Grt-A'-017 core	Grt-A'-018 core
SiO_2	38.07	38.07	38.07	38.07	38.07	38.07	38.07	38.07
TiO_2	0.127	0.024	0.864	0.231	0.034	0.017	0.069	0.055
Al_2O_3	9.695	8.995	12.94	10.80	10.38	9.985	10.61	9.878
FeO	17.07	17.65	13.14	15.79	16.48	16.80	15.93	16.96
MnO	0.874	0.913	1.170	0.898	0.920	0.968	0.975	0.973
MgO	0.048	0.045	0.043	0.053	0.016	0.037	0.058	0.033
CaO	34.98	34.76	34.66	35.46	35.06	35.22	34.96	34.91
Number of cations on the basis of 12 oxygens								
Si	2.981	2.981	2.973	2.970	2.988	2.977	2.990	2.992
Ti	0.007	0.001	0.050	0.013	0.002	0.001	0.004	0.003
Al	0.896	0.841	1.174	0.986	0.953	0.920	0.976	0.909
Cr	0.000	0.000	0.000	0.000	0.000	0.000	0.000	0.000
Fe^{3+}	1.112	1.170	0.809	1.020	1.054	1.095	1.028	1.094
Fe^{2+}	0.008	0.000	0.036	0.003	0.020	0.004	0.011	0.014
Mn	0.058	0.061	0.076	0.059	0.061	0.064	0.064	0.064
Mg	0.005	0.005	0.005	0.006	0.002	0.004	0.000	0.004
Ca	2.940	2.952	2.859	2.941	2.927	2.950	2.923	2.922
Ura	0.000	0.000	0.000	0.000	0.000	0.000	0.000	0.000
Gro	42.25	39.66	55.24	46.90	44.74	43.28	45.93	42.66
And	55.37	58.14	40.82	50.85	52.51	54.34	51.32	54.60
Spe	1.930	2.030	2.560	1.960	2.020	2.120	2.140	2.140
Alm	0.270	0.000	1.210	0.090	0.670	0.120	0.380	0.470
Pyr	0.190	0.18	0.170	0.200	0.060	0.140	0.220	0.130

(c)

Sample	Grt-D-024 rim	Grt-D-025 rim	Grt-D-026 rim	Grt-D-027 rim	Grt-D-028 rim	Grt-D-029 Core	Grt-D-030 Core
SiO_2	37.36	37.36	37.36	37.36	37.36	37.36	37.36
TiO_2	0.031	0.131	0.000	0.019	0.000	1.678	1.712
Al_2O_3	9.289	8.604	5.363	7.511	7.265	7.798	8.513
FeO	17.84	18.56	22.37	20.05	20.08	18.18	17.58
MnO	0.889	0.921	0.494	0.707	0.731	0.687	0.755
MgO	0.000	0.055	0.039	0.066	0.061	0.112	0.093
CaO	34.93	34.42	34.94	34.61	34.72	34.10	35.09
Number of cations on the basis of 12 oxygens							
Si	2.975	2.977	2.977	2.971	2.982	2.952	2.923
Ti	0.002	0.008	0.000	0.001	0.000	0.101	0.101
Al	0.861	0.803	0.506	0.705	0.681	0.733	0.791
Cr	0.000	0.000	0.000	0.000	0.000	0.000	0.000

Table 1 (*Continued*)

(c)

Sample	Grt-D-024 rim	Grt-D-025 rim	Grt-D-026 rim	Grt-D-027 rim	Grt-D-028 rim	Grt-D-029 Core	Grt-D-030 Core
Fe^{3+}	1.154	1.206	1.499	1.314	1.331	1.213	1.159
Fe^{2+}	0.019	0.023	0.000	0.021	0.004	0.000	0.000
Mn	0.059	0.062	0.033	0.048	0.049	0.046	0.050
Mg	0.000	0.006	0.005	0.008	0.007	0.013	0.011
Ca	2.944	2.922	2.999	2.952	2.957	2.915	2.965
Ura	0.000	0.000	0.000	0.000	0.000	0.000	0.000
And	57.26	60.02	74.04	65.1	66.17	61.18	57.46
Gro	40.13	36.94	24.71	32.38	31.83	36.81	40.51
Alm	0.650	0.780	0.000	0.680	0.130	0.000	0.000
Pyr	0.000	0.220	0.150	0.260	0.240	0.450	0.360
Spe	1.960	2.050	1.100	1.570	1.630	1.560	1.670

(d)

Sample	Grt-Cn-012 rim	Grt-Cn-013 rim	Grt-Cn-014 rim	Grt-Cn-015 rim	Grt-Cn-016 rim	Grt-Cn-017 core	Grt-Cn-019 core	Grt-Cn-20 core	Grt-Cn-21 core
SiO_2	38.02	38.02	38.02	38.02	38.02	38.02	38.02	38.02	38.02
TiO_2	0.010	0.002	0.041	0.170	0.017	0.444	0.535	0.356	0.285
Al_2O_3	6.410	6.350	7.304	9.278	6.689	11.18	10.33	9.811	9.805
FeO	20.93	21.02	20.74	18.15	20.63	15.73	16.79	17.00	17.69
MnO	0.620	0.630	0.700	0.820	0.670	1.040	1.240	1.130	1.060
MgO	0.038	0.025	0.037	0.055	0.064	0.100	0.076	0.081	0.099
CaO	35.34	35.27	34.84	35.20	34.91	34.71	34.16	34.35	34.50
Number of cations on the basis of 12 oxygens									
Si	3.0074	2.980	2.981	2.962	2.980	2.963	2.962	2.992	2.954
Ti	0.0007	0.000	0.002	0.010	0.001	0.026	0.031	0.021	0.017
Al	0.5945	0.595	0.677	0.854	0.628	1.024	0.954	0.904	0.907
Cr	0.0000	0.000	0.000	0.000	0.000	0.000	0.000	0.000	0.000
Fe^{3+}	1.3774	1.398	1.334	1.164	1.375	0.983	1.051	1.087	1.113
Fe^{2+}	0.0000	0.000	0.030	0.021	0.000	0.039	0.049	0.025	0.048
Mn	0.0415	0.042	0.047	0.054	0.045	0.068	0.082	0.075	0.071
Mg	0.0045	0.003	0.004	0.006	0.007	0.012	0.009	0.009	0.012
Ca	2.9800	3.005	2.935	2.946	2.980	2.891	2.866	2.878	2.899
Ura	0.00	0.000	0.000	0.000	0.000	0.000	0.000	0.000	0.000
And	68.28	68.73	66.34	57.68	68.00	48.98	52.42	54.59	55.11
Gro	30.20	29.78	30.97	39.63	30.27	47.06	42.92	41.76	40.60
Alm	0.00	0.000	1.000	0.700	0.000	1.300	1.640	0.830	1.570
Pyr	0.15	0.100	0.140	0.210	0.250	0.380	0.300	0.320	0.380
Spe	1.37	1.380	1.550	1.780	1.48	2.270	2.730	2.510	2.330

(e)

Sample	Grt-Cs-030 rim	Grt-Cs-031 core	Grt-Cs-032 rim
SiO_2	37.54	38.36	37.84
TiO_2	0.000	0.070	0.149
Al_2O_3	9.290	10.75	8.441
FeO	18.32	16.27	18.85
MnO	0.711	0.731	0.643
MgO	0.000	0.014	0.006
CaO	35.02	35.17	34.79
Number of cations on the basis of 12 oxygens			
Si	2.957	2.982	2.984
Ti	0.000	0.004	0.009
Al	0.862	0.985	0.785
Cr	0.000	0.000	0.000
Fe^{3+}	1.166	1.024	1.220
Fe^{2+}	0.040	0.034	0.023
Mn	0.047	0.048	0.043
Mg	0.000	0.002	0.001
Ca	2.955	2.930	2.940
Ura	0.000	0.000	0.000
And	57.5	50.97	60.86
Gro	39.62	46.25	36.90
Alm	1.330	1.130	0.780
Pyr	0.000	0.050	0.020
Spe	1.560	1.600	1.430

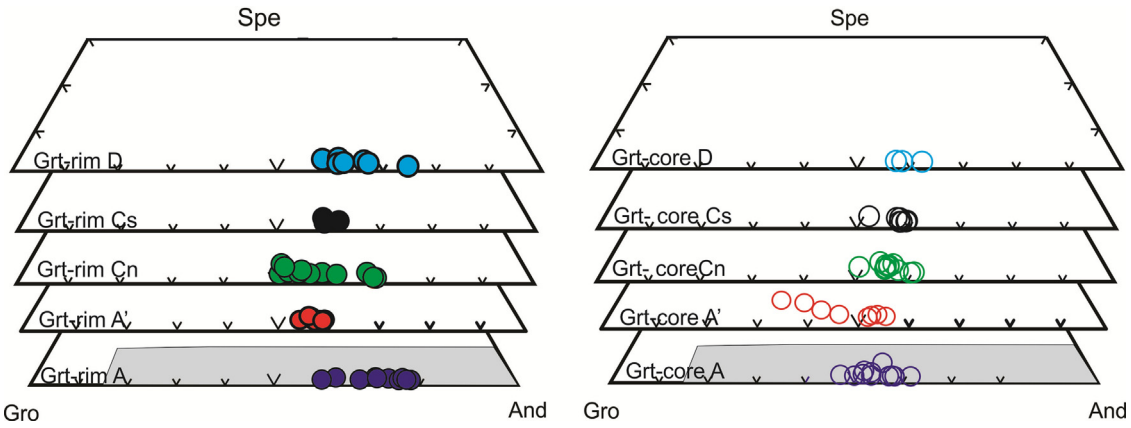

Fig. 4. Ternary diagram summarizing the compositional variations in garnet from different Sangan skarn zones. Abbreviations: Gro = grossular; And = andradite; Spe = almandine + spessartine. Diagram modified after Meinert et al. (2005). Garnet rim from A: filled violet circle; Garnet core from A: violet circle; Garnet rim from A': filled red circle; Garnet core from A': red circle; Garnet rim from Cn: filled green circle; Garnet core from Cn: green circle; Garnet rim from Cs: filled black circle; Garnet core from Cs: circle; Garnet rim from D: filled blue circle; Garnet core from D: light blue circle. (For interpretation of the references to color in this figure legend, the reader is referred to the web version of this article.)

(Fig. 5k, l, n, o). Similar to other reported oscillatory grandites (*e.g.*, San Benito, Armbruster et al., 1998; Galore Creek, Russell et al., 1999), garnet from the Sangan deposits are principally classified as low-Ti garnet, with Ti content less than 1 wt.%.

Chemical compositions of clinopyroxene grains from Sangan skarns are reported in Table 2. In some places, pyroxene from the Sangan skarns shows zonation patterns with a rim more Fe-rich than the core (Mazaheri, 1996). Clinopyroxene from skarn associated with A' orebody shows a binary diopside-hedenbergite composition, ranging from Hd_{29} to Hd_{77} (Table 4). It has MgO and FeO contents of 3.20–11.5 wt.% and 8.15–19.9 wt.% (Table 4), respectively. Other constituents, such as MnO (up to 0.85 wt.%), Al_2O_3, and Na_2O are generally less than 1.1 wt.% (Table 2) and the Mn/Fe ratios are relatively restricted (<0.05). The composition of clinopyroxene crystals from the Sangan iron deposit plots in the field of skarn deposits on the johanssonite-diopside-hedenbergite ternary diagram (Fig. 6). Like with garnet, the clinopyroxene has high Fe/Fe + Mg ratios (0.28–0.77) and low TiO_2 (0.08), MnO (0.19–0.89%) contents (Table 2).

Representative magnetite analyses from A, B, Cs and Cn are listed in Table 3 and presented in Fig. 7. Magnetite in the Cs orebody has high MgO (3.15–3.33 wt.%) and low SiO_2 (<0.024 wt.%) and MnO (0.09–0.13) contents. In addition, this magnetite has low Al_2O_3 (0.32–0.39 wt.%) content. Magnetite in the A, B, and Cn orebodies contains moderate to low MgO (0.03–1.01 wt.% in sample A-3; up to 0.03 wt.% in sample B-2, and 0.02–0.22 wt.% in sample Cn-1,) moderate to high SiO_2 (0.06–3.43 wt.% for A, B, and Cn), low MnO (0.01–0.12 wt.%, for A, B, and Cn) and low to moderate Al_2O_3 (0.05–0.43 wt.%) contents (Table 3). In a Ca + Al + Mn *versus* Ti + V discriminant diagram (Dupuis and Beaudoin 2011), magnetite from Sangan plots dominantly in the skarn field (Fig. 7).

5.2. Trace and rare earth element compositions

Garnet, clinopyroxene and magnetite from calc-silicate and magnetite dominated stages in the Sangan skarn mineralization were analyzed for their trace element contents. Each of these minerals shows a range of characteristic patterns for REE. To some extent, these patterns reflect typical patterns for each mineral, with trends and LREE/HREE fractionation controlled by crystal structural parameters intrinsic to each mineral group. Chondrite-normalized REE patterns are summarized in Fig. 8. Garnet is the major REE-host in the silicate dominated stage but a calculation for typical multi-component skarn (garnet and pyroxene, 25%), using average REE concentrations in these minerals, shows that garnet account for >90% of ΣREE. Garnet grains from all of the skarn are characterized by similar REE patterns from core to rim; a depletion of LREE relative to HREE and positive Eu anomalies (Fig. 8). The exception is garnet from the Cn orebody where cores are more enriched in LREE and depleted in HREE than the rim (Chondrite value Sun and McDonough, 1989). The results of LA-ICP-MS analyses show that all garnet crystals in Sangan skarn are depleted in large ion lithophile elements (LILE; *e.g.*, Rb, Ba, La, Sr) and enriched in high field strength elements (HFSE; *e.g.*, U, Th, Pb, Sm, Nd; Fig. 8; Table 4). Variations in La_N/Yb_N (chondrite normalized La/Nb ratios) *versus* $Fe^{3+}/(Fe^{3+} + Al)$ have been discussed in the literature (*e.g.*, Peng et al., 2014) to study of LREE/HREE fractionation between a hydrothermal fluid and a growing garnet. Within the garnets from different orebodies in Sangan (Fig. 9a), LREE/HREE fractionation does not increase with increasing Fe contents from core to rim. Also, Eu/Eu* *vs* $Fe^{3+}/(Fe^{3+} + Al)$ ratios and ΣREE *vs* Al concentrations do not show any correlations (Fig. 9b, c). Al-rich garnet cores from A, Cs and Cn orebodies are generally more Zr-, Hf- and Nb-enriched, and Rb-, Ba- and Y-depleted than Fe-rich garnet rims, while garnets from D orebodies generally show similar contents of these elements from core to rim. These results also show that garnet rims from A' orebody are Hf- enriched and Y-depleted compared to garnet cores (Table 4; Fig. 9d–i).

In-situ LA-ICP-MS analysis showed that clinopyroxene cores have higher contents of REE compared to their rims (Fig. 10). They also have distinct REE patterns from core to rim. In general, clinopyroxene cores are HREE-rich, have relatively high ΣREE, low ΣLREE/ΣHREE ratios, as well as positive Eu anomalies (Fig. 10). In contrast, pyroxene rims are LREE-rich, have relatively low ΣREE, high ΣLREE/ΣHREE ratios and lack Eu anomalies (Fig. 10; Table 5).

Magnetite grains from the Sangan skarns were analyzed for REE and trace elements by LA-ICP-MS. The results show that magnetite from the Sangan Fe deposit contains substantial U, Ti, and Cu, but these concentrations vary significantly, as illustrated by the concentration of U (0.01–1.61 ppm), Ti (2.96–180.6 ppm), and Cu (0.03–63.87 ppm), *etc.* In addition, there is a spatial variation within individual magnetite grains from Sangan, which has been observed in many iron deposits, such as the Los Colorados iron oxide-apatite deposit, Chile (Knipping et al., 2015), porphyry Cu-Mo-Au deposits in British Columbia, Canada (Canil et al., 2016) and the Chengchao iron deposit, China (Hu et al., 2014) and others. The magnetite grains from Sangan contain 0.03 to 64 ppm Cu, 1328 to 5026 ppm Si, and ~3 to 180 ppm Ti. The U values (~0.01–1.6 ppm) of

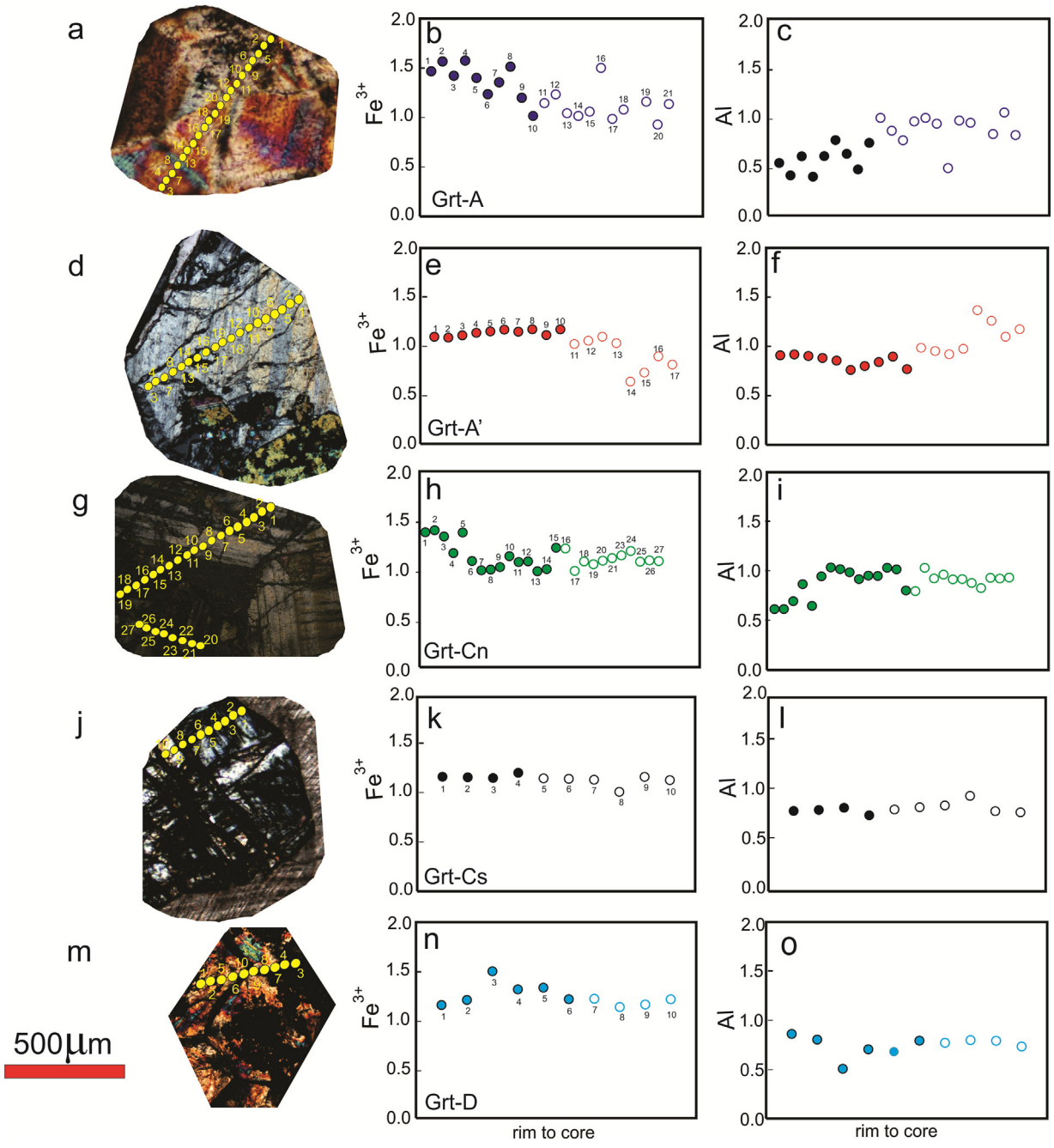

Fig. 5. Garnet morphology and associated compositional variations from Sangan. Garnets from A and Cn orebodies show more Fe-enriched cores and Al-depleted rims than those from other types of skarn. Symbols as in Fig. 4.

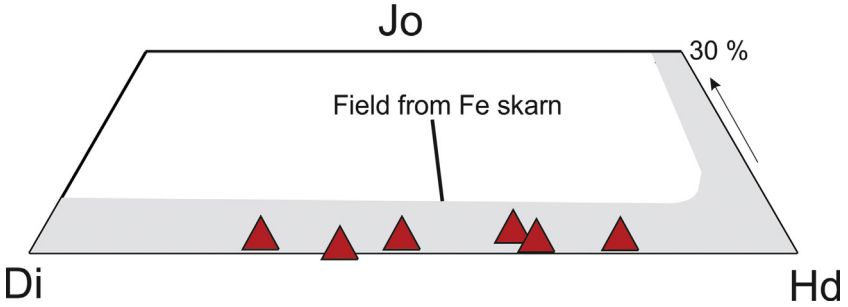

Fig. 6. Johannsenite (Jo) – Diopside (Di) – Hedernbergite (Hd) ternary diagram (Meinert et al., 2005) showing the composition of pyroxenes from the Sangan A' skarn iron deposit.

Table 2
Selected electron micro probe analyses of pyroxene from Sangan orebody.

	CPx-A'-1	CPx-A'-2	CPx-A'-3	CPx-A'-5	CPx-A'-6	CPx-A'-7	CPx-A'-8
SiO_2	50.2	49.6	48.5	49.5	49.7	50.9	50.8
TiO_2	0.08	0.08	0.08	0.08	0.08	0.08	0.08
Al_2O_3	0.10	0.09	0.18	0.10	0.60	1.30	0.55
Cr_2O_3	0.10	0.18	0.11	0.11	0.16	0.10	0.10
Fe_2O_3	4.30	2.60	3.36	4.90	4.99	3.38	3.49
FeO	16.2	16.9	19.9	15.8	10.8	8.15	10.3
MnO	0.19	0.69	0.85	0.34	0.42	0.28	0.32
MgO	5.66	5.68	3.20	5.20	8.27	11.5	9.78
CaO	22.4	23.7	23.2	22.5	24.8	23.2	24.5
Na_2O	1.06	0.25	0.40	1.05	0.35	0.44	0.30
K_2O	0.05	0.05	0.05	0.05	0.05	0.05	0.05
Total	100	99.8	99.8	99.5	100	99.3	100
Mn/Fe^{2+}	0.01	0.03	0.04	0.01	0.02	0.03	0.03
$CaMgSi_2O_6$	33.2	33.7	19.3	31.0	48.2	64.2	55.8
$CaFeSi_2O_6$	66.1	63.6	76.9	67.9	47.5	29.1	40.6
$CaMnSi_2O_6$	0.64	2.30	2.90	0.00	1.39	0.89	1.04

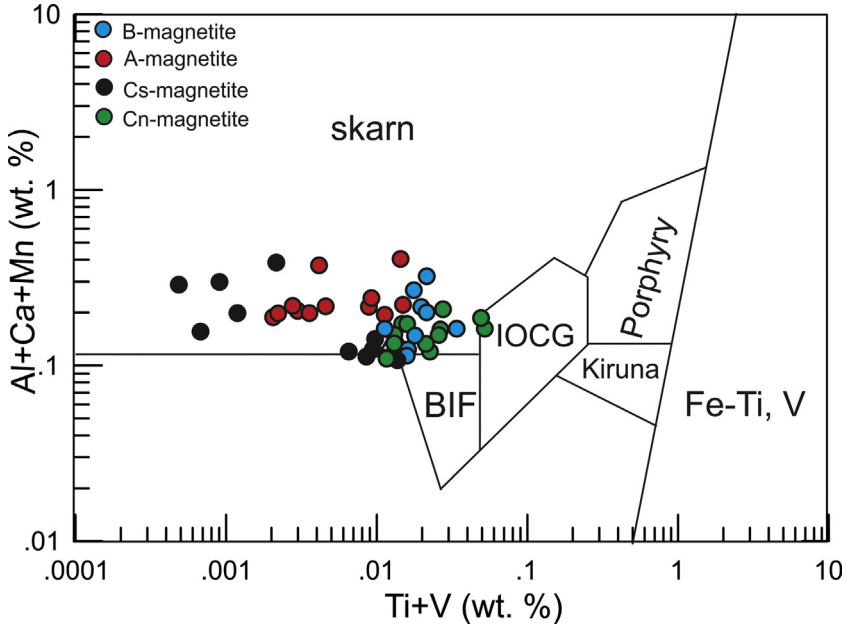

Fig. 7. Position of magnetite samples from the Sangan on Al + Ca + Mn *vs.* Ti + V discriminant diagram (Dupuis and Beaudoin, 2011).

magnetite grains (Table 6) are higher than to those from pyroxenes (up to 0.08 ppm; Table 5) and significantly lower than those from garnets (1.1–8.8 ppm) (Table 4; Fig. 13). Chondrite-normalized REE patterns for magnetite from the Sangan skarn are characterized by slight enrichment in LREEs relative to HREEs (Fig. 11a). Magnetite grains from the Cs orbody have Ba, Th, La, Nd, Sm, Y, Dy, Yb, and Lu contents higher than those from other types of iron ores (Fig. 11b).

5.3. *Baro-acoustic decrepitation results of fluid inclusions*

Fluid inclusions are trapped in garnet, quartz, calcite and opaque minerals of the Sangan skarn. To find the temperature of hydrothermal fluid during garnet and quartz formation in the silicate-dominant stage we used the baro-acoustic decrepitation method. One garnetite sample (A-1) was chosen from the skarn associated with orebody A. The garnet has only low decrepitation intensity with two distinct peaks near 450° and 500 °C (Fig. 12) which are consistent with the results of microthermometric studies by Mazaheri (1996), from garnet (450–500 °C) in the silicate-dominant stage. It is not clear why there are 2 peaks on the decrepigram, which may be due to different fluid events or to fluid inclusion size variations. Mazaheri (1996) described that fluid inclusions in garnet have wide variations in size and shape from less than 3 μm to 10 μm and from rod –like, elongated to irregular, respectively. The garnet formation temperature is estimated to be about 450 °C and above. The baro-acoustic decrepitation data from the opaque minerals provides the best estimate of the formation temperatures of these deposits (Burlinson, 1984). In this study, two magnetite samples (B-4 and C-4) were chosen from high-grade orebodies B and C. The analysis of sample B-4 shows broad, low intensity decrepitation with an onset temperature of 400 °C and peaks at 450 °C and 600 °C. The decrepitation intensity of this sample is low in comparison with magnetite from other skarn deposits (Burlinson, 2001), suggesting either a low abundance of fluid inclusions or later removal events such as recrystallization. The presence of two separate peaks may indicate multiple fluid events but may also be caused by the size distribution of inclusions formed in a single fluid event. The sample formation temperature is estimated to be about 400 °C. The analysis of sample C-4 shows an intense, single, high temperature peak at 790 °C. The formation temperature of sample C-4 is also estimated to be about 400 °C. There were insufficient samples in this study to understand the significance of the different shapes of the decrepigram peaks or the dual peaks in samples A-1 and B-4. However it is notable that no samples had

Table 3
(a) Selected electron micro probe analyses of magnetite from Cn orebody. (b) Selected electron micro probe analyses of magnetite from Cs orebody. (c) Selected electron micro probe analyses of magnetite from A orebody. (d) Selected electron micro probe analyses of magnetite from B orebody.

(a)

Sample Number	Mt-Cn Cn-1-1	Mt-Cn Cn-1-2	Mt-Cn Cn-1-3	Mt-Cn Cn-1-4	Mt-Cn Cn-1-5	Mt-Cn Cn-1-6	Mt-Cn Cn-1-7	Mt-Cn Cn-1-8	Mt-Cn Cn-1-9	Mt-Cn Cn-1-10
SiO_2	0.635	0.814	0.309	0.19	0.692	0.105	0.123	0.142	0.135	0.062
TiO_2	0.052	0.053	0.053	0.035	0.051	0.110	0.137	0.098	0.054	0.047
Al_2O_3	0.258	0.283	0.315	0.191	0.295	0.286	0.276	0.253	0.162	0.118
Cr_2O_3	0.001	0.002	0.001	0.003	0.001	0.001	0.006	0.007	0.002	0.002
V_2O_3	0.010	0.011	0.002	0.001	0.002	0.010	0.017	0.012	0.023	0.005
Fe_2O_3	67.53	66.58	67.52	67.74	67.78	69.40	68.77	67.71	68.82	68.64
FeO	31.71	31.53	31.00	30.94	31.91	31.78	31.50	31.11	31.42	31.09
MnO	0.025	0.046	0.051	0.027	0.034	0.060	0.039	0.015	0.017	0.028
MgO	0.227	0.261	0.103	0.074	0.225	0.033	0.072	0.019	0.035	0.043
CaO	0.032	0.109	0.080	0.020	0.071	0.031	0.002	0.004	0.001	0.003
ZnO	0.000	0.018	0.000	0.000	0.016	0.000	0.013	0.000	0.002	0.006
Total	100.4	99.72	99.53	99.23	101.0	101.8	100.9	99.37	100.7	100.1
Number of cations on the basis of 32 oxygens										
Si	0.194	0.249	0.095	0.059	0.209	0.031	0.037	0.043	0.041	0.019
Ti	0.012	0.052	0.052	0.011	0.011	0.024	0.031	0.022	0.012	0.011
Al	0.127	0.102	0.114	0.069	0.10	0.101	0.190	0.122	0.078	0.063
Cr	0.000	0.000	0.000	0.000	0.000	0.000	0.001	0.001	0.000	0.000
V	0.002	0.002	0.000	0.001	0.000	0.002	0.004	0.003	0.006	0.001
$Fe^{(iii)}$	15.49	15.37	15.66	15.79	15.45	15.78	15.75	15.77	15.83	15.89
$Fe^{(ii)}$	8.085	8.090	8.020	8.0191	8.084	8.016	8.022	8.053	8.032	8.000
Mn	0.006	0.011	0.013	0.010	0.017	0.015	0.010	0.004	0.014	0.013
Zn	0.000	0.00	0.000	0.000	0.003	0.000	0.002	0.000	0.000	0.001
Mg	0.103	0.119	0.047	0.034	0.101	0.014	0.032	0.009	0.016	0.019
Ca	0.030	0.045	0.046	0.026	0.030	0.040	0.035	0.023	0.023	0.001
Si	0.194	0.249	0.095	0.058	0.209	0.031	0.037	0.044	0.041	0.019
Al	0.127	0.10	0.114	0.069	0.105	0.101	0.190	0.78	0.06	0.123
Ti/V	6.000	26.00	–	11.00	–	12.00	8.000	22.00	2.000	–

Mt-Cn: Magnetite from Cn orebody;

(b)

Sample Number	Mt-Cs Cs-3-1	Mt-Cs Cs-3-2	Mt-Cs CS-3-3	Mt-Cs CS-3-4	Mt-Cs CS-3-5	Mt-Cs CS-3-6	Mt-Cs CS-3-7	Mt-Cs CS-3-8	Mt-Cs CS-3-9	Mt-Cs CS-3-10
SiO_2	0.024	0.009	0.014	0.005	0.000	0.018	0.012	0.022	0.003	0.003
TiO_2	0.010	0.011	0.013	0.014	0.010	0.025	0.007	0.008	0.011	0.011
Al_2O_3	0.393	0.358	0.360	0.371	0.322	0.343	0.343	0.327	0.322	0.322
Cr_2O_3	0.000	0.000	0000	0.000	0.000	0.000	0.004	0.003	0.005	0.005
V_2O_3	0.000	0.018	0.012	0.007	0.008	0.008	0.010	0.016	0.002	0.002
Fe_2O3	70.74	71.16	71.07	71.03	70.96	71.67	71.28	70.58	70.05	70.05
FeO	26.39	26.22	26.29	26.16	26.29	26.62	26.44	26.10	25.73	25.73
MnO	0.121	0.128	0.112	0.124	0.132	0.141	0.144	0.126	0.092	0.092
MgO	3.153	3.302	3.274	3.333	3.201	3.234	3.207	3.231	3.327	3.327
CaO	0.025	0.051	0.032	0.025	0.032	0.035	0.041	0.052	0.010	0.010
ZnO	0.011	0.019	0.007	0.002	0.008	0.000	0.005	0.004	0.000	0.001
Total	100.8	101.2	101.1	101.0	100.9	102.1	101.5	100.4	99.56	99.55
Number of cations on the basis of 32 oxygens										
Si	0.007	0.002	0.004	0.001	0.000	0.005	0.003	0.006	0.000	0.000
Ti	0.002	0.002	0.002	0.003	0.002	0.005	0.001	0.001	0.002	0.002
Al	0.137	0.124	0.125	0.129	0.112	0.118	0.119	0.115	0.114	0.114
Cr	0.000	0.000	0.000	0.000	0.000	0.000	0.000	0.001	0.001	0.001
V	0.000	0.004	0.002	0.001	0.001	0.001	0.002	0.003	0.000	0.000
Fe(iii)	15.84	15.86	15.85	15.85	15.88	15.85	15.86	15.86	15.87	15.87
Fe(ii)	6.569	6.494	6.519	6.490	6.537	6.547	6.540	6.520	6.482	6.482
Mn	0.050	0.032	0.028	0.031	0.033	0.035	0.036	0.031	0.023	0.023
Zn	0.002	0.004	0.001	0.000	0.001	0.000	0.001	0.001	0.000	0.000
Mg	1.399	1.457	1.447	1.474	1.419	1.417	1.414	1.438	1.493	1.493
Ca	0.008	0.016	0.010	0.007	0.010	0.011	0.013	0.016	0.003	0.003
Si	0.007	0.002	0.004	0.001	0.000	0.005	0.003	0.006	0.000	0.000
Al	0.137	0.124	0.125	0.129	0.112	0.118	0.119	0.115	0.114	0.114
Ti/V	–	0.500	1.000	3.000	2.000	5.000	0.500	0.250	–	–

Mt-Cs: Magnetite from Cs orebody

(c)

Sample Number	Mt-A A-3-1	Mt-A A-3-2	Mt-A A-3-3	Mt-A A-3-4	Mt-A A-3-5	Mt-A A-3-6	Mt-A A-3-7	Mt-A A-3-8	Mt-A A-3-9	Mt-A A-3-10	Mt-A A-3-11	Mt-A A-3-12
SiO_2	0.314	0.520	0.193	1.148	0.474	1.399	3.432	0.314	0.520	0.193	0.835	1.127
TiO_2	0.032	0.027	0.034	0.021	0.055	0.041	0.000	0.032	0.027	0.034	0.000	0.000
Al_2O_3	0.056	0.054	0.050	0.074	0.055	0.116	0.153	0.056	0.054	0.050	0.096	0.080
Cr_2O_3	0.000	0.011	0.000	0.000	0.006	0.004	0.001	0.000	0.011	0.000	0.006	0.000

Table 3 (*Continued*)

(c)

Sample Number	Mt-A A-3-1	Mt-A A-3-2	Mt-A A-3-3	Mt-A A-3-4	Mt-A A-3-5	Mt-A A-3-6	Mt-A A-3-7	Mt-A A-3-8	Mt-A A-3-9	Mt-A A-3-10	Mt-A A-3-11	Mt-A A-3-12
V_2O_3	0.004	0.015	0.007	0.007	0.005	0.002	0.005	0.004	0.015	0.007	0.000	0.002
Fe_2O_3	67.59	68.09	68.79	65.71	68.05	65.71	61.49	67.59	68.09	68.79	67.67	66.19
FeO	30.85	31.40	30.98	31.76	31.44	32.19	33.61	30.85	31.40	30.98	31.26	31.24
MnO	0.091	0.090	0.071	0.098	0.081	0.085	0.120	0.091	0.090	0.071	0.080	0.102
MgO	0.036	0.056	0.071	0.160	0.061	0.264	1.013	0.036	0.056	0.071	0.134	0.160
CaO	0.200	0.298	0.261	0.200	0.199	0.190	0.348	0.200	0.298	0.261	0.728	0.699
ZnO	0.000	0.000	0.003	0.000	0.008	0.004	0.000	0.000	0.000	0.003	0.000	0.001
Total	99.17	100.5	100.4	99.19	100.4	99.97	100.1	99.17	100.5	100.4	100.8	99.61
Number of cations on the basis of 32 oxygens												
Si	0.097	0.158	0.059	0.354	0.144	0.427	1.029	0.097	0.158	0.059	0.253	0.345
Ti	0.008	0.006	0.007	0.004	0.012	0.008	0.000	0.007	0.006	0.007	0.000	0.000
Al	0.020	0.019	0.018	0.026	0.019	0.041	0.054	0.020	0.019	0.018	0.034	0.028
Cr	0.000	0.002	0.000	0.000	0.001	0.000	0.000	0.000	0.002	0.000	0.001	0.000
V	0.001	0.003	0.001	0.001	0.001	0.002	0.001	0.000	0.003	0.001	0.000	0.000
$Fe^{(iii)}$	15.76	15.64	15.84	15.2	15.66	15.10	13.88	15.76	15.64	15.84	15.45	15.27
$Fe^{(ii)}$	7.997	8.018	7.929	8.193	8.041	8.222	8.434	7.997	8.018	7.929	7.935	8.016
Mn	0.023	0.023	0.018	0.025	0.020	0.021	0.030	0.023	0.023	0.018	0.020	0.026
Zn	0.000	0.000	0.000	0.000	0.001	0.000	0.000	0.000	0.000	0.000	0.000	0.000
Mg	0.016	0.025	0.032	0.073	0.027	0.120	0.453	0.016	0.025	0.032	0.060	0.073
Ca	0.066	0.097	0.085	0.066	0.065	0.062	0.111	0.066	0.097	0.085	0.236	0.229
Si	0.097	0.158	0.059	0.354	0.144	0.427	1.029	0.097	0.158	0.059	0.253	0.345
Al	0.020	0.019	0.018	0.026	0.019	0.041	0.054	0.020	0.019	0.018	0.034	0.028
Ti/V	8.000	2.000	7.000	4.000	11.00	4.000	0.000	7.000	2.000	7.000	0.000	0.000

Mt-A: Magnetite from A orebody

(d)

Sample Number	Mt-B B-2-1	Mt-B B-2-2	Mt-B B-2-3	Mt-B B-2-4	Mt-B B-2-5	Mt-B B-2-6	Mt-B B-2-7	Mt-B B-2-8	Mt-B B-2-9	Mt-B B-2-10	Mt-B B-2-11	Mt-B B-2-12
SiO_2	0.779	1.393	1.393	0.615	1.688	1.500	1.318	1.153	0.694	0.846	0.906	0.915
TiO_2	0.002	0.001	0.001	0.001	0.001	0.001	0.034	0.049	0.000	0.000	0.000	0.000
Al_2O_3	0.392	0.439	0.439	0.221	0.377	0.341	0.161	0.164	0.137	0.248	0.248	0.225
Cr_2O_3	0.000	0.000	0.000	0.000	0.001	0.007	0.000	0.001	0.000	0.004	0.004	0.000
V_2O_3	0.001	0.001	0.001	0.000	0.003	0.002	0.000	0.000	0.000	0.000	0.000	0.009
Fe_2O_3	66.29	64.92	64.92	67.22	64.83	64.83	65.77	65.76	68.47	66.99	67.02	68.03
FeO	31.86	32.71	32.71	31.67	33.05	32.80	32.74	32.30	32.25	32.06	32.26	32.73
MnO	0.021	0.038	0.038	0.028	0.041	0.026	0.030	0.038	0.027	0.050	0.029	0.042
MgO	0.000	0.006	0.006	0.003	0.023	0.027	0.015	0.016	0.000	0.018	0.006	0.018
CaO	0.065	0.065	0.065	0.125	0.251	0.098	0.095	0.125	0.215	0.154	0.149	0.115
ZnO	0.000	0.000	0.000	0.003	0.016	0.000	0.000	0.000	0.001	0.000	0.000	0.000
Total	99.42	99.57	99.57	99.90	100.2	99.63	100.1	99.58	101.8	100.3	100.6	102.0
Number of cations on the basis of 32 oxygens												
Si	0.240	0.427	0.427	0.188	0.513	0.459	0.402	0.354	0.209	0.258	0.275	0.275
Ti	0.001	0.001	0.001	0.0001	0.002	0.001	0.007	0.011	0.008	0.003	0.002	0.001
Al	0.142	0.158	0.158	0.080	0.135	0.123	0.057	0.059	0.049	0.089	0.089	0.079
Cr	0.000	0.000	0.000	0.000	0.000	0.001	0.000	0.000	0.000	0.001	0.000	0.001
V	0.001	0.001	0.001	0.001	0.001	0.001	0.002	0.001	0.001	0.001	0.001	0.002
$Fe^{(iii)}$	15.37	14.98	14.98	15.54	14.83	14.95	15.12	15.21	15.53	15.39	15.35	15.37
$Fe^{(ii)}$	8.213	8.393	8.393	8.138	8.407	8.408	8.364	8.307	8.133	8.187	8.217	8.219
Mn	0.0052	0.009	0.009	0.007	0.010	0.006	0.007	0.019	0.019	0.013	0.014	0.011
Zn	0.000	0.000	0.000	0.000	0.003	0.000	0.000	0.013	0.000	0.012	0.003	0.011
Mg	0.0000	0.002	0.002	0.001	0.010	0.012	0.018	0.041	0.069	0.050	0.049	0.037
Ca	0.021	0.021	0.021	0.041	0.081	0.032	0.031	0.355	0.209	0.258	0.276	0.275
Si	0.240	0.427	0.427	0.188	0.513	0.459	0.402	0.059	0.049	0.089	0.089	0.079
Ti/V	1.000	1.000	1.000	1.000	2.000	1.000	3.500	11.00	8.000	3.000	2.000	1.000

Mt-B: Magnetite from B orebody

low temperature decrepitation (below 300 °C) commonly caused by CO_2 rich fluids (Burlinson, 1984, 2012) and therefore we tentatively suggest that these deposits were formed from fluids with very low CO_2 contents (Fig. 12).

6. Discussion

As discussed in Section 5.1, major element compositions of minerals, the garnet and pyroxene from the Sangan skarn are andradite-grossularite, and diopside-hedenbergite, respectively. Due to their similar Mg/(Mg + Fe) ratios (1.00–1.08 and 1.00–1.50 for garnet and pyroxene, respectively), it is inferred that these minerals were formed in equilibrium at the same temperatures. Using the garnet-clinopyroxene geothermometer based on garnet-clinopyroxene Fe^{2+}-Mg^{2+} distribution between garnet and pyroxene (Ravna, 2000), it is calculated that these mineral pairs in the Sangan skarn equilibrated at temperatures of 500–600 °C. The calc-silicate dominant stage was formed at temperatures around 350–400 °C as indicated by mineral chemistry and the decrepitation analysis of garnet sample A-1 (Fig. 12). In addition, decrepitation data of the magnetite samples in the same diagram (Fig. 12) show that sample B-4 has broad, low intensity decrepitation with peaks at 450 °C and 600 °C, perhaps indicating a multi-stage fluid event. The decrepitation analysis of sample

Table 4
Selected LA-ICP-MS analyses of garnet from Sangan skarn.

Sample (ppm)	A-011 core	A-04 core	A-05 core	A-06 core	A-07 core	A-08 rim	A-09 rim	A-010 rim
Ca	230798.5	231921.7	228343.1	232377.2	224126.5	226408.2	227266.6	229988.9
Sc	5.378138	5.467443	2.203846	1.327666	1.138141	1.298890	0.506061	1.312782
Ti	5179.811	5230.487	3534.300	2344.550	1327.924	641.9432	128.6585	3566.747
Fe^{3+}	100421.1	102235.1	97441.48	100496.6	94172.54	135487.3	140590.3	104332.9
Fe^{2+}	97352.70	97669.33	93053.17	96677.15	90818.68	130725.9	135783.1	100330.8
Cu	0.112127	0.112127	0.116096	0.106174	0.110143	0.090297	0.101212	0.117089
Rb	0.248069	0.140407	0.146857	0.015281	0.030264	0.026097	0.091091	0.069459
Sr	2.341772	0.391949	0.779929	0.054178	0.187540	0.281806	0.53186	0.829543
Y	17.24576	17.14653	15.22152	16.05503	10.77612	42.78695	7.203926	16.80916
Zr	101.4007	106.759	136.2197	99.13833	60.31055	38.54001	21.01641	97.49115
Nb	18.62503	19.73638	17.73198	15.83673	11.26234	12.07600	7.104698	21.43317
Mo	1.552912	1.295913	1.410025	1.379264	1.287975	1.274083	1.268129	1.307820
Ba	4.901845	0.397903	1.49933	0.052591	0.129988	0.207386	0.188533	0.309590
La	0.028379	0.048622	0.066284	0.090793	0.132767	0.092282	0.052491	0.458432
Ce	0.310582	0.308598	0.630095	1.08555	1.364380	0.937701	0.459424	3.373739
Pr	0.118180	0.141598	0.258984	0.425687	0.502092	0.425687	0.258984	1.075628
Nd	1.590619	1.699769	2.679146	4.157638	4.614085	5.487288	4.108024	9.079328
Sm	1.554897	1.668016	1.970661	2.679146	2.470768	5.85443	6.578792	3.711113
Eu	1.429870	1.455669	2.168124	2.460845	2.579918	4.127869	5.358292	2.589841
Gd	2.391386	2.460845	2.421154	2.808142	2.282236	7.442072	8.225971	3.314203
Tb	0.485223	0.451486	0.401872	0.478277	0.364165	1.218515	0.929763	0.539798
Dy	3.006597	3.01652	2.718837	2.937138	2.292158	7.610759	3.274512	3.026443
Ho	0.656887	0.634065	0.577505	0.588420	0.400880	1.609472	0.319513	0.637041
Er	1.891279	1.826781	1.554897	1.651148	1.082573	4.435475	0.468354	1.655117
Tm	0.277837	0.27883	0.236162	0.2441	0.168389	0.603304	0.048026	0.226239
Yb	1.964707	1.913109	1.634279	1.6958	1.099442	3.959183	0.303637	1.733507
Lu	0.296691	0.270891	0.235169	0.238146	0.152414	0.480262	0.041576	0.218301
Hf	5.854430	5.844508	5.139991	2.629532	1.35148	0.784891	0.335389	2.292158
Ta	2.530305	2.560073	2.033174	0.829543	0.545752	0.385995	0.061918	2.450923
W	3.750804	3.711113	6.469642	6.777247	8.58319	1.159971	0.251046	17.90066
^{204}Pb	0.922817	1.061736	0.972431	0.952585	1.012122	1.002199	0.873203	0.992276
^{206}Pb	0.248069	0.452478	0.511022	0.074421	0.096251	0.071444	0.029768	0.240131
^{207}Pb	0.173648	0.437594	0.433625	0.033737	0.029768	0.069459	0.029768	0.071444
^{208}Pb	0.171664	0.377065	0.470339	0.017563	0.022624	0.04753	0.022227	0.031654
^{232}Th	0.036417	0.03979	0.036714	0.098731	0.067971	0.441563	0.161543	0.112127
^{238}U	2.877601	2.778374	3.324126	3.522581	3.552349	1.30782	0.832520	8.821336

Sample (ppm)	CN-013 rim	CN-014 rim	CN-015 rim	CN-016 rim	CN-017 core	CN-018 core	CN-019 core	CN-020 core
Ca	233474	232823.6	230633.4	228321.6	223670.2	225049.7	227103.7	230992.8
Sc	1.736889	0.324166	0.851436	3.381731	2.645354	3.791941	3.081577	4.562335
Ti	1793.688	48.85501	1176.642	3748.969	2541.631	2065.747	1593.736	1690.625
Fe^{3+}	126210.1	128001.7	130970.3	131599	126137.5	125807.8	128834.9	134190
Fe^{2+}	122688.2	124730.5	127524	128622.4	123645.7	123603	127591.8	132702.8
Cu	0.09705	0.115059	0.11706	0.108055	0.119061	0.104053	0.101052	0.100051
Rb	0.016508	0.017909	0.083143	0.031316	0.016709	0.014507	0.016609	0.015908
Sr	0.070736	0.089246	0.124564	0.099551	0.065233	0.046724	0.055729	0.063132
Y	41.37118	21.79115	20.10029	32.79679	15.45791	14.82759	10.90558	10.87557
Zr	27.41403	1.278654	18.86966	30.35554	68.43503	88.15512	89.24568	119.191
Nb	12.96664	5.092607	4.722417	10.46536	7.493836	5.903021	6.163155	7.093631
Mo	1.151589	0.926474	1.314673	1.382708	1.568803	1.611825	1.309670	0.99651
Ba	0.05803	0.115059	0.121062	0.075038	0.05903	0.046024	0.062032	0.047024
La	0.005903	0.007404	0.008204	0.008604	0.010906	0.017109	0.041521	0.046524
Ce	0.056629	0.043822	0.088545	0.096449	0.341175	0.619317	0.768393	0.965494
Pr	0.047224	0.032016	0.050526	0.05823	0.174589	0.345177	0.427219	0.502257
Nd	0.779399	0.505259	0.973498	1.012518	2.941506	5.582858	6.133139	7.533856
Sm	2.191122	1.074550	2.191122	1.954000	3.171623	4.342223	4.882499	4.892504
Eu	1.263647	0.274140	1.221625	1.483759	2.46126	2.451255	2.391224	2.241147
Gd	6.293221	2.551306	4.522315	3.811951	3.741915	4.062079	3.781936	3.781936
Tb	1.384709	0.647331	0.803411	0.757388	0.627321	0.620318	0.491251	0.494253
Dy	8.344271	4.102100	4.402253	4.932525	3.271675	3.121598	2.541301	2.611337
Ho	1.554796	0.824422	0.737377	1.185607	0.572293	0.54728	0.403206	0.428219
Er	3.611849	1.943995	1.700871	3.271675	1.298665	1.241636	0.884453	1.000512
Tm	0.459235	0.228117	0.214110	0.517265	0.165985	0.175090	0.123063	0.119361
Yb	2.971521	1.466751	1.395714	3.69189	1.091559	1.182605	0.778398	0.803411
Lu	0.426218	0.193099	0.179492	0.554284	0.150177	0.162083	0.105354	0.097750
Hf	0.805412	0.021111	0.458235	1.869957	2.421239	2.941506	2.271162	3.341710
Ta	0.357183	0.008004	0.187096	0.780399	0.693355	0.598306	0.339174	0.370189
W	0.806413	1.185607	0.214110	0.195100	0.033017	0.021811	0.039920	0.036018
^{204}Pb	0.870446	0.980502	0.850435	0.920471	0.880451	1.080553	0.980502	0.790405
^{206}Pb	0.046024	0.034818	0.060031	0.062032	0.037019	0.050026	0.107055	0.108055
^{207}Pb	0.047524	0.049425	0.049025	0.039020	0.034017	0.027014	0.037019	0.088045
^{208}Pb	0.014007	0.015108	0.065734	0.061832	0.017909	0.015808	0.013107	0.018309
^{232}Th	0.065233	0.043722	0.029315	0.030516	0.159081	0.175090	0.186095	0.253130
^{238}U	0.565289	0.049025	0.238122	1.160594	1.432733	2.151101	2.321188	2.981526

Table 4 (*Continued*)

Sample (ppm)	D-024	D-025	D-026	D-027	D-028	D-029	D-030
Ca	227545.3	229870.1	232009.6	230531.2	234830.6	231380.7	229319.2
Sc	0.493615	0.388402	0.535897	0.389386	0.357920	0.506398	0.343171
Ti	599.8802	395.9542	525.6904	382.5617	385.4231	378.0975	430.0353
Fe^{3+}	136091.9	137319.3	138920.6	136681.7	136194.2	137118.2	1383740
Fe^{2+}	135587.6	136708.7	138385.0	136762.3	136404.6	137176.0	138467.2
Cu	0.099313	0.091447	0.095380	0.115046	0.101280	0.096363	0.099313
Rb	0.061456	0.016323	0.015143	0.014946	0.026942	0.013668	0.082105
Sr	0.329405	0.048575	0.079352	0.031269	0.073846	0.036677	0.318588
Y	23.49097	21.88820	23.68763	21.59321	22.12419	20.84590	24.82826
Zr	24.71026	15.02478	20.16743	13.90382	13.27451	14.37581	11.62257
Nb	8.741514	7.659887	7.866379	7.276401	6.558593	3.638200	5.653960
Mo	0.970515	0.984281	1.091460	1.062944	1.209456	1.090477	0.968548
Ba	1.594908	0.058998	0.036382	0.040315	0.062931	0.058998	1.097360
La	0.053688	0.055163	0.053000	0.052606	0.080040	0.039135	0.048280
Ce	0.933149	1.128825	0.874151	1.003947	0.873168	0.748289	0.863335
Pr	0.503448	0.637177	0.496565	0.553596	0.512298	0.407085	0.480832
Nd	7.345231	8.830010	7.178071	7.974542	7.600889	6.332435	7.089574
Sm	7.581223	8.426858	7.453394	8.338362	7.591056	6.371767	7.178071
Eu	6.037446	6.430765	5.929283	6.293103	5.948949	5.358971	5.634294
Gd	7.207570	7.335398	7.296066	7.266568	7.522225	6.155442	6.322602
Tb	1.004930	0.965598	0.993130	1.000997	0.972481	0.859402	0.891851
Dy	5.014817	4.877155	5.181977	4.857489	4.906654	4.424838	4.719827
Ho	0.892834	0.824986	0.847602	0.828920	0.843669	0.751239	0.870218
Er	1.946929	1.740436	1.907597	1.81910	1.730603	1.819100	2.212419
Tm	0.240908	0.228125	0.225175	0.205509	0.226158	0.209442	0.267457
Yb	1.390382	1.275337	1.304836	1.252721	1.272387	1.346134	1.622441
Lu	0.167161	0.147691	0.176994	0.151428	0.164211	0.161261	0.229108
Hf	0.061259	0.016618	0.129795	0.030974	0.019371	0.028024	0.018683
Ta	0.067454	0.033727	0.060276	0.030581	0.033825	0.037169	0.039037
W	0.533930	0.578179	0.291056	0.494599	0.570312	0.077680	0.374636
^{204}Pb	0.963631	0.737473	0.776805	0.894801	0.865302	0.894801	0.934133
^{206}Pb	0.214359	0.160277	0.141595	0.196659	0.402169	0.101280	0.922333
^{207}Pb	0.104230	0.031466	0.080630	0.084564	0.335304	0.026549	0.819087
^{208}Pb	0.097445	0.015929	0.049853	0.082499	0.281223	0.013570	0.796471
^{232}Th	0.109441	0.135695	0.099116	0.100296	0.072567	0.047395	0.103050
^{238}U	5.496632	6.352101	4.788658	5.516298	5.103313	3.402209	4.631331

Sample (ppm)	A'-011 rim	A'-012 rim	A'-013 rim	A'-014 core	A'-015 core	A'-016 core	A'-017 core	A'-018 core
Ca	226252.0	227004.7	229023.2	228116.5	233707.4	232994.4	230432.8	233002.4
Sc	0.973857	0.567082	0.978867	2.028869	2.253297	6.562516	12.38362	9.628363
Ti	1038.721	4217.053	2204.965	115.3700	134.8372	125.2388	521.5948	279.0021
Fe^{3+}	113275.9	101647.3	107986.4	120303.5	123494.5	127825.0	125579.8	126800.3
Fe^{2+}	111783.5	100354.2	106603.2	118684.1	121833.9	125962.3	124113.8	124779.7
Cu	0.090172	0.096183	0.104199	0.100191	0.082157	0.095182	0.113216	0.101193
Rb	0.024547	0.058912	0.014127	0.017834	0.013125	0.012624	0.020038	0.016031
Sr	0.079051	0.140869	0.065124	0.028154	0.042481	0.043082	0.127543	0.163512
Y	17.50338	33.81449	19.00625	13.17513	14.77818	9.648401	13.06492	11.24144
Zr	122.4034	114.7488	109.1782	100.0107	134.3462	108.9879	129.7875	162.2895
Nb	13.26530	31.68042	18.52533	5.610700	7.965191	3.025771	8.085420	5.710892
Mo	1.183257	1.405681	1.552962	1.446759	1.246377	1.228343	1.407685	1.224335
Ba	0.048092	0.168321	0.055105	0.039075	0.047090	0.051097	0.151289	0.051097
La	0.065826	0.047791	0.036570	0.033263	0.090372	0.027252	0.043683	0.059213
Ce	0.672282	0.726385	0.493942	0.556060	1.067035	0.632206	0.932779	1.034974
Pr	0.313598	0.342653	0.237453	0.318608	0.504963	0.327625	0.458875	0.530011
Nd	4.067758	4.759076	3.276248	4.338274	6.572535	4.789134	6.121675	6.802974
Sm	3.697051	4.338274	3.186076	4.047720	5.430356	4.187987	4.729019	5.420337
Eu	2.995713	3.166038	2.552869	2.975675	3.707070	3.446573	3.446573	4.087796
Gd	3.767185	4.989516	3.646955	3.867376	4.729019	4.177968	4.458503	4.809172
Tb	0.609162	0.862645	0.564076	0.566080	0.652244	0.567082	0.590125	0.631204
Dy	3.456592	5.470433	3.366420	2.955637	3.376439	2.694138	3.005732	2.985694
Ho	0.667273	1.191272	0.673284	0.516986	0.578103	0.408780	0.493942	0.452864
Er	1.689222	3.386458	1.936694	1.201291	1.300480	0.806538	1.251387	0.952817
Tm	0.248875	0.509973	0.294562	0.166818	0.157300	0.091174	0.154394	0.112615
Yb	1.654155	3.797242	1.984785	1.000909	1.024955	0.649238	0.999907	0.713360
Lu	0.204089	0.509973	0.272520	0.138965	0.139967	0.093178	0.130048	0.091675
Hf	2.604968	2.533832	2.358498	2.445664	2.905541	2.584930	3.957548	3.526726
Ta	0.287548	1.239364	0.722378	0.021541	0.019136	0.005210	0.049795	0.023345
W	3.045809	4.729019	3.396478	0.444848	2.755255	0.590125	2.735216	4.228064
^{204}Pb	0.821567	0.761452	0.801529	1.041987	0.871662	0.801529	0.971853	0.701338
^{206}Pb	0.106203	0.221422	0.111212	0.037071	0.094180	0.071236	0.115220	0.091174
^{207}Pb	0.040076	0.070134	0.033063	0.048392	0.032061	0.031059	0.042080	0.039976
^{208}Pb	0.017934	0.037872	0.021641	0.018836	0.020940	0.016131	0.022042	0.015530
^{232}Th	2.200196	0.094981	1.758353	0.571089	2.584930	0.886691	2.835408	2.060930
^{238}U	3.005732	6.111656	2.875484	1.309497	2.875484	1.499860	3.035790	3.316325

Table 4 (*Continued*)

Sample (ppm)	Cs-030 rim	Cs-031 core	Cs-032 rim
Ca	232828.4	226401.8	233225.5
Sc	0.941367	13.11332	0.425809
Ti	145.5927	420.0051	149.6713
Fe^{3+}	132691.8	113340.9	132422.3
Fe^{2+}	130230.9	111618.6	131121.3
Cu	0.091743	0.089749	0.088752
Rb	0.046769	0.013861	0.011767
Sr	0.097128	0.040686	0.058636
Y	30.69414	16.34428	22.24777
Zr	20.76192	44.71492	43.95704
Nb	1.770049	4.078591	4.597141
Mo	0.98325	1.164742	1.041088
Ba	0.139609	0.051855	0.050858
La	0.005584	0.005285	0.011368
Ce	0.047268	0.033506	0.059234
Pr	0.033805	0.035800	0.040387
Nd	0.587357	0.551457	0.880537
Sm	2.009379	1.692266	2.473082
Eu	1.694261	0.975272	2.038298
Gd	6.272454	4.178312	6.800976
Tb	1.248508	0.749902	1.234547
Dy	7.249721	4.048675	6.212622
Ho	1.160753	0.644198	0.905467
Er	2.662552	1.415042	1.768054
Tm	0.296172	0.170024	0.191365
Yb	1.657364	1.060035	1.071004
Lu	0.195653	0.127842	0.120064
Hf	0.734944	1.572601	1.472880
Ta	0.024132	0.071201	0.025728
W	0.196450	0.609296	0.754888
^{204}Pb	0.797768	0.777824	0.907462
^{206}Pb	0.084763	0.066813	0.026127
^{207}Pb	0.035900	0.033905	0.036498
^{208}Pb	0.038492	0.033506	0.017451
^{232}Th	0.007379	0.044476	0.018748
^{238}U	0.216395	0.185481	0.441764

C-4 shows a single, intense, high temperature peak at 790 °C, the interpretation of which is unclear. The magnetite dominant stage was formed at a temperature of about 400 °C. Lack of any low-temperature peak around 300 °C, shows an absence of CO_2-rich fluid inclusions (Sośnicka et al., 2015) which is consistent with studies by Mazaheri (1996) who showed that garnet from a silicate-dominant stage was formed from hydrothermal fluid with low CO_2 ($X_{CO2} < 0.07$) content.

Anisotropic garnets from Sangan have a wide range in composition (Fig. 4) mainly reflecting major-element heterogeneity of the protolith. Gaspar et al. (2008) showed that variations within a single sample are due to the existence of chemical potentials controlled by fluid pathways at small scale (centimeter or less). In addition, minerals from skarn are able to record numerous geological processes including variations of physicochemical conditions and hydrothermal fluid evolution. In this contribution, major, trace and rare earth element (REE) concentrations of garnet, pyroxene and magnetite from the Sangan iron skarn deposit are important for the investigation of hydrothermal fluid evolution.

In the following section, we consider the origin and evolution of hydrothermal fluids responsible for garnet, pyroxene and magnetite formation based on (1) Controls on compositional variation of garnets, pyroxene and magnetite, and (2) Implications for the hydrothermal fluid evolution of the skarn.

6.1. Controls on compositional variation of garnets, pyroxene and magnetite

Garnet has the chemical formula $X_3Y_2Z_3O_{12}$, where X is a divalent cation such as Ca, Mg, Mn or Fe in eight-fold, dodecahedral coordination, which is replaced by Zn, Y, Na, Li, Be, B, F, Sc, Cu, Ga, Ge, Sr, Nb, Ag, Cd, In, U and REE^{3+} (Gaspar et al., 2008). The Y is the trivalent cation site which includes Fe, Al or Cr in octahedral coordination that is substituted by Ti, V, Fe^{2+}, Zr and Sn. Z is Si in tetrahedral coordination which is incorporated by Al, Ti, and Fe^{3+} site (*e.g.*, Menzer, 1926; Dziggel et al., 2009; Gaspar et al., 2008; Smith et al., 2004). The incorporation of REE in garnet has been widely discussed in the literature (*e.g.*, Gaspar et al., 2008; Ismail et al., 2014; Smith et al., 2004). The partitioning of REE between a hydrothermal fluid and a growing garnet is mainly controlled by crystal chemistry, crystal-liquid equilibrium (*e.g.*, P, T, fluid composition, complexation), growth rate and surface adsorption (*e.g.*, Smith et al., 2004). Gaspar et al. (2008), in a study of gold skarn garnets from Crown Jewel, North America, explained the REE incorporation in terms of ionic radii relative to that of Ca, and showed that REE incorporation could be correlated with changes in major element composition. Garnets from the Crown Jewel, North America gold skarn (Gaspar et al., 2008), Ocna de Fier Fe-skarn (Nicolescu et al., 1999) and Isle of Skye (Smith et al., 2004) deposit are andradite-rich and show enrichment in LREE and depletion in HREE. In these deposits REE patterns are strongly HREE-enriched when garnets are more grossular-rich. In the Sangan iron skarn, REE patterns (Fig. 8) also show that grossular-rich garnets are in general enriched in HREE and depleted in LREE. A La_N/Yb_N *versus* $Fe^{3+}/(Fe^{3+} + Al)$ diagram (Fig. 9a) shows that LREE/HREE fractionation does not increase with increasing Fe-content. The ionic radius and charge disparity between the host cation and its substituent, at a given site, exert the principal control on substitution mechanisms (Goldschmidt's first rule). In this case, REE only incorporate X^{2+} cations in the dodecahedral position. Incorporation of $(REE)^{3+}$ by replacement of X^{2+} cations requires coupled substitution to maintain charge balance. There are four mechanisms to maintain charge

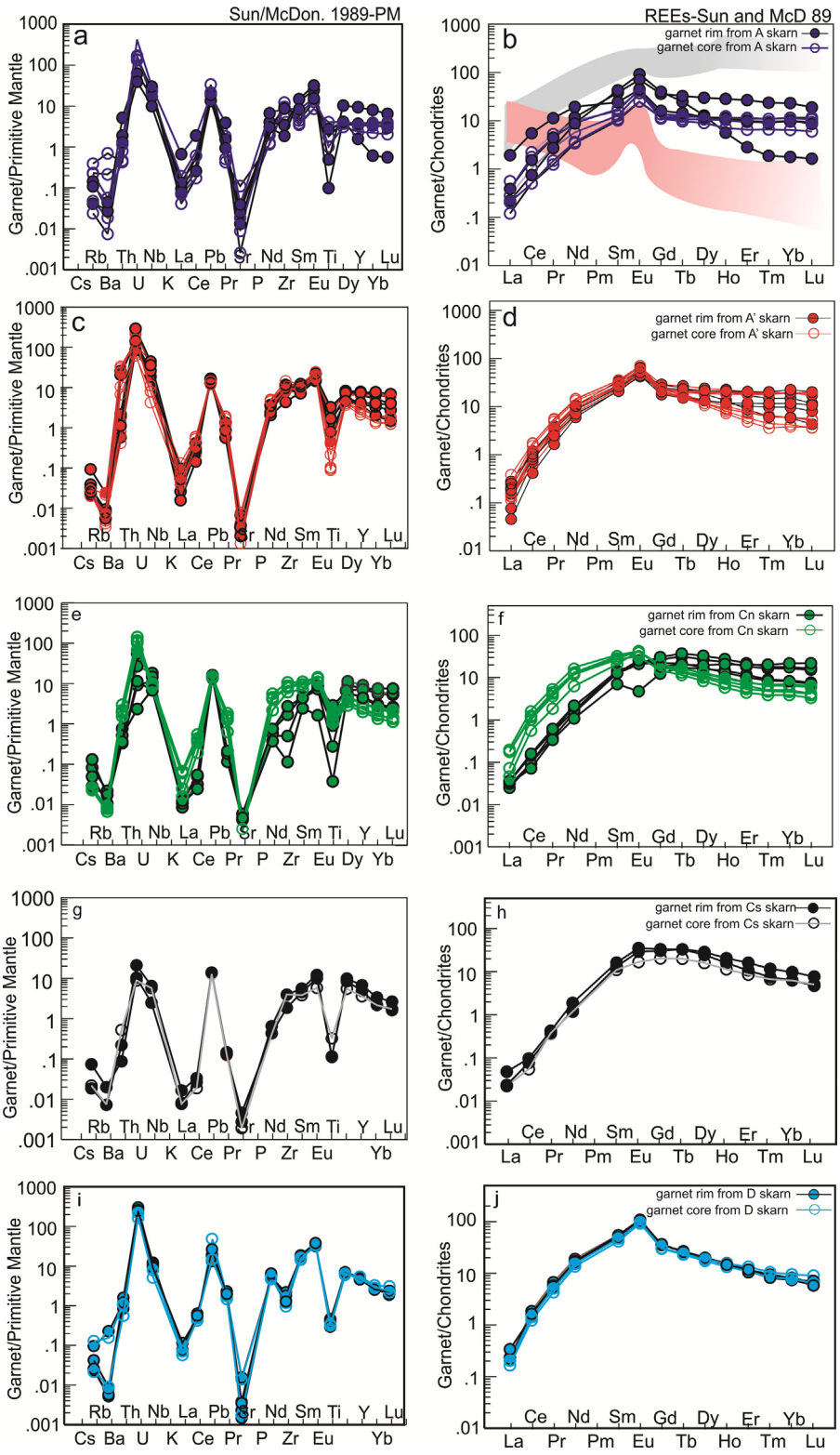

Fig. 8. Trace element spider diagram of Sangan garnets are shown on the left. Chondrite-normalized REE fractionation patterns of Sangan garnets (Chondrite value Sun and McDonough, 1989) (right). Symbols as in Fig. 4. Results from Ismail et al. (2014) and Zhai et al. (2014) are shown by red and gray field for comparition. (For interpretation of the references to color in this figure legend, the reader is referred to the web version of this article.)

balance including: (i) substitution of a trivalent cation into the Z (Si) site as 'yttrogarnet' (YAG)-type substitution (Jaffe, 1951); (ii) incorporation of a monovalent cation (essentially Na^+/Li^+) into the X site (Enami et al., 1995); (iii) charge compensation *via* vacancies in the dodecahedral site or; (iv) by substitution of divalent cations (Mg^{2+}, Fe^{2+}) into the Y site (as in menzerite; Grew et al., 2010). Garnets from the Sangan deposit contain low Na concentrations, indicating that they did not undergo Na^+–REE^{3+} coupled substitution (Table 4; Gaspar et al., 2008). The high Al_2O_3 (4.32–12.94 wt.%) along high REE values, might indicate they underwent REE^{3+}–Ca^{2+}

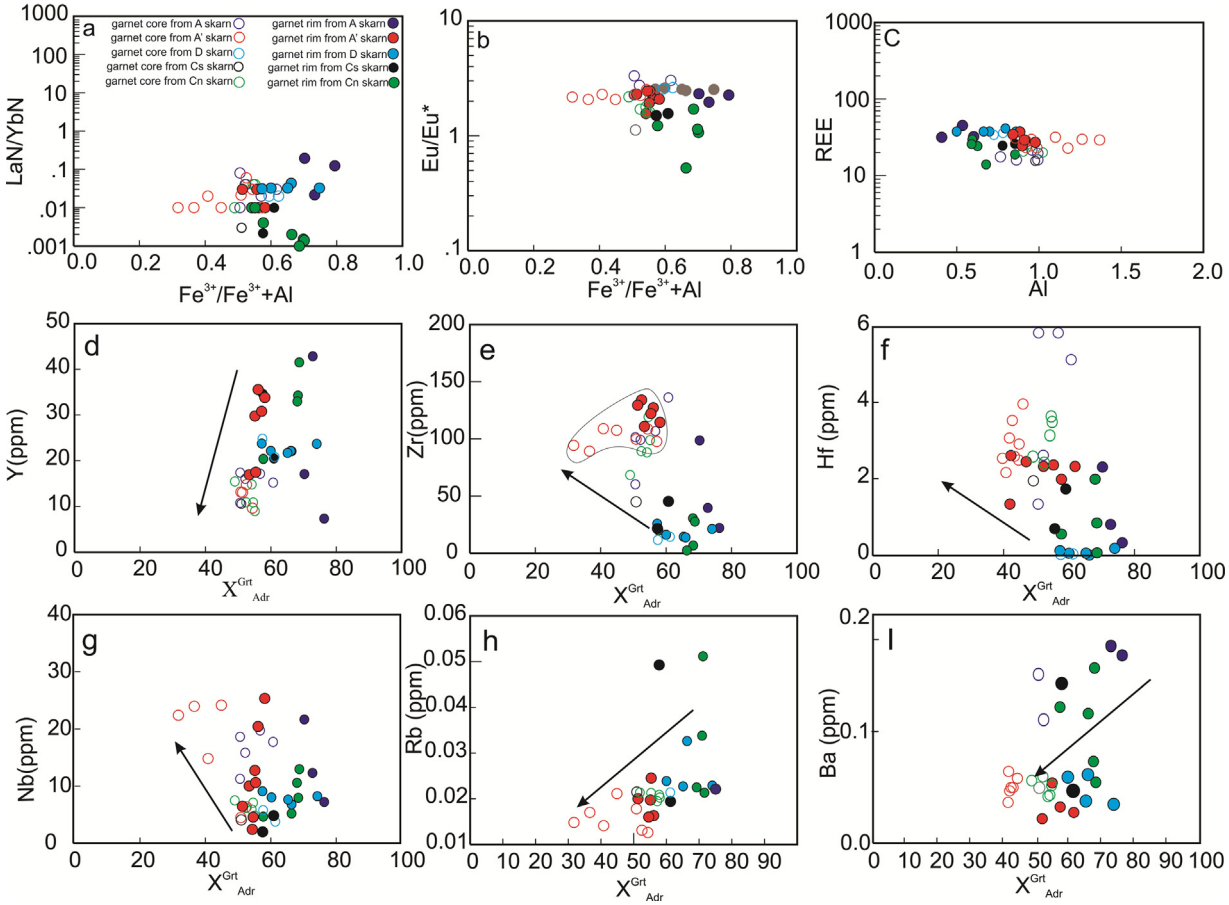

Fig. 9. (a) LREE/HREE fractionation as a function of $Fe^{3+}/(Fe^{3+}+Al)$ ratio (in atoms per formula unit) of garnets from the Sangan deposit; (b) Eu anomaly as a function of $Fe^{3+}/(Fe^{3+}+Al)$ ratio; (c) Total REE concentrations *versus* total Al (in atoms per formula unit) for garnets from the Sangan deposit; (d)–(i) The variation of trace-element composition of garnets from the Sangan deposit with increasing And and/or decreasing Gro components from rim to core; (in atoms per formula unit). Symbols as in Fig. 4.

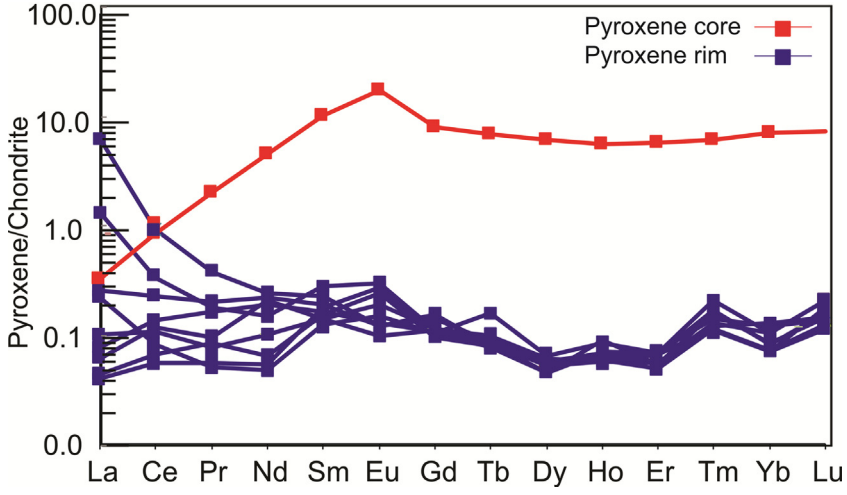

Fig. 10. Chondrite-normalized REE fractionation patterns of the Sangan pyroxene (Chondrite values after Sun and McDonough, 1989).

and Al^{+3}- Si^{+4} coupled substitutions. Other mechanisms such as charge compensation *via* vacancies in the dodecahedral site are difficult to evaluate but cannot be completely ruled out.

Large ion lithophile elements (LILE) have larger ionic sizes compared with the octahedral and eight coordination sites within the garnet structure (Gaspar et al., 2008), and so, as expected, all garnets from the Sangan skarns are extremely LILE-depleted (Fig. 8a, c, e, g, i). In comparison, variations in some HFSE in correlation with Al suggest that substitution of these elements for Al^{3+} can occur in the garnet lattice (Fig. 9d–i).

Pyroxene has the chemical formula $XY(Si,Al)_2O_6$ where X is divalent cations (Ca, Mg, Mn, or Fe) in eightfold coordination, Y is trivalent cations (Fe, Al, and Cr) in octahedral coordination. Trace elements such as REE^{3+} may incorporate into pyroxene by replacement of Ca^{2+} in the X-site (Ismail et al., 2014). To achieve charge balance, coupled substitution involving vacancies (*e.g.* van Orman

Table 5
Selected LA-ICP-MS analyses of pyroxene from Sangan skarn.

	A'-019	A'-020	A'-021	A'-022	A'-023	A'-024	A'-025	A'-026	A'-027	A'-028
Si	242628.1	241743.2	241193.9	234611	246872.6	241696	240410.3	306867.9	242883.7	241961.7
Ca	168067	168067	168067	168067	168067	168067	168067	168067	168067	168067
Sc	2.151687	3.065273	1.827171	2.693725	2.278672	2.64199	2.305715	5.984748	3.006484	3.703724
Ti	27.79557	40.39999	78.01337	32.39289	51.39358	44.92676	52.60464	1056.573	37.4958	52.55761
Fe^{3+}	126021.8	106572.8	147719.4	108981.3	126799.2	115584.1	129143.1	270707.5	111833.9	112709.9
Fe^{2+}	124287.4	105139.1	145379.1	107506.6	124592.0	113992.3	127069.8	266507.3	110388.9	111789.9
Cu	0.531455	0.497357	0.189301	0.158731	3.809545	0.424459	0.365669	2.037636	0.23986	0.277485
Rb	0.164257	0.325693	0.008701	1.078195	0.263376	1.640221	0.475017	18.65972	1.216938	0.14568
Sr	4.291617	4.185796	4.632595	4.7149	4.632595	6.419789	4.185796	18.89487	4.891268	3.703724
Y	0.035038	0.009524	0.01458	0.005173	0.028924	0.026925	0.020811	1.9083	0.01846	0.007172
Zr	0.75603	1.333341	1.164028	1.208707	1.782491	1.146391	0.791304	14.32107	0.91241	0.94298
Nb	0.010229	0.013169	0.005056	0.005526	0.026925	0.00776	0.008466	2.627881	0.00776	0.007525
Mo	1.071141	0.961793	1.061734	0.880663	1.002945	0.911234	0.941804	1.073492	0.937101	0.932398
Ba	1.415646	0.959441	0.023516	1.836577	3.786029	3.268684	0.827753	92.67541	0.993539	0.739569
La	0.33745	0.063492	0.009524	0.018577	1.630814	0.014697	0.010347	0.200119	0.024574	0.053498
Ce	0.212935	0.145562	0.034098	0.087008	0.594947	0.072899	0.04127	0.673725	0.06749	0.050794
Pr	0.017637	0.019636	0.005291	0.016226	0.038095	0.009289	0.008172	0.137449	0.007525	0.004938
Nd	0.071135	0.106526	0.025397	0.090418	0.118754	0.100059	0.030688	0.895949	0.048678	0.022928
Sm	0.04515	0.029983	0.027866	0.02575	0.036449	0.022458	0.024221	0.380955	0.02234	0.0194
Eu	0.017872	0.007172	0.016226	0.00776	0.007172	0.011523	0.01458	0.363318	0.005761	0.008818
Gd	0.023045	0.032217	0.021047	0.02234	0.029395	0.023868	0.019871	0.41858	0.023281	0.022105
Tb	0.003222	0.003057	0.003269	0.002963	0.003292	0.003763	0.003081	0.0816	0.003527	0.006114
Dy	0.01164	0.014109	0.013404	0.01164	0.013639	0.01552	0.014815	0.54674	0.01458	0.016579
Ho	0.005173	0.003304	0.003645	0.004115	0.003292	0.003292	0.003998	0.087361	0.00341	0.004938
Er	0.009171	0.009289	0.011875	0.011523	0.011052	0.011288	0.008936	0.185774	0.008348	0.01164
Tm	0.003175	0.003327	0.003645	0.002928	0.002998	0.004468	0.004233	0.012111	0.002975	0.005409
Yb	0.022458	0.01799	0.021399	0.012111	0.012111	0.014227	0.014697	0.084657	0.012816	0.018107
Lu	0.003763	0.005409	0.003586	0.002939	0.004703	0.004115	0.003763	0.010582	0.003292	0.005409
Hf	0.03786	0.053851	0.034451	0.076661	0.065256	0.033392	0.040565	0.659616	0.057496	0.037155
Ta	0.005879	0.002798	0.003034	0.00281	0.003763	0.003527	0.002857	0.05244	0.003645	0.003645
W	0.028101	0.033863	0.017637	0.029747	0.026338	0.423283	0.092534	0.09759	0.021634	0.040447
^{204}Pb	2.257508	0.858323	0.529103	0.764261	7.419207	3.315715	2.116414	2.480907	1.528521	1.011176
^{206}Pb	2.727822	0.338626	0.020106	0.92064	7.901279	4.279859	1.590838	1.994132	1.955331	0.470314
^{207}Pb	2.527939	0.343329	0.024927	0.805413	7.395691	3.927124	1.473259	1.769557	1.895366	0.464435
^{208}Pb	2.645517	0.312759	0.011875	0.872433	7.607332	4.091734	1.519115	1.96121	1.889487	0.429162
Th	0.043269	0.037037	0.003763	0.036332	0.076779	0.030923	0.016696	0.088184	0.022458	0.013404
U	0.080424	0.043974	0.003998	0.010347	0.04856	0.008936	0.007878	0.16414	0.025044	0.018342

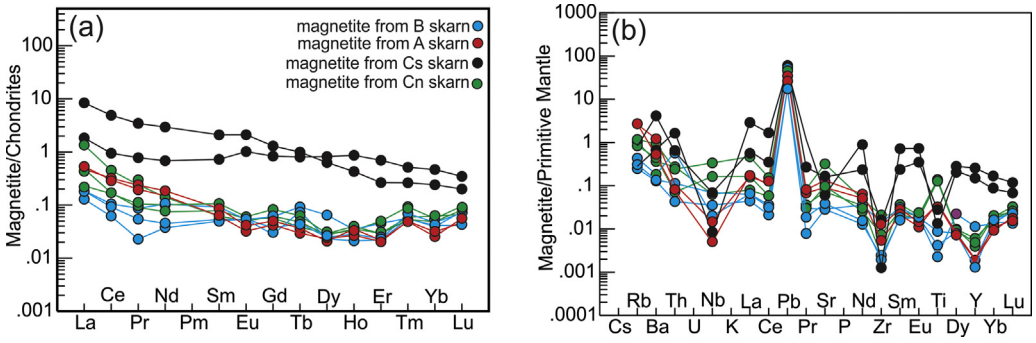

Fig. 11. (a) Primitive mantle-normalized REE patterns of the Sangan magnetite; (b) Chondrite-normalized multi-elemental patterns of magnetite from the Sangan Fe skarn. Chondrite values after Sun and McDonough (1989). Symbols as in Fig. 8.

et al., 2001), as well as coupled substitution involving monovalent cations (*e.g.* Na^+) has been proposed (Ismail et al., 2014). Pyroxene from the Sangan deposit contains low Na concentrations, indicating that they have not incorporated Na^+ into the X site. The presence of Al_2O_3 might also suggest charge balance *via* compensation for REE^{3+} incorporation into the Ca site by Al^{3+} incorporation into the Si site similar to pyroxene from Hillside iron oxide-copper-gold deposit, Yorke Peninsula, South Australia (Ismail et al., 2014). To attain charge equilibrium, coupled replacements involving Al has been proposed by Al^{3+} incorporation into the Si site (Ismail et al., 2014). The trace element data on pyroxene also suggest that pyroxene rims possibly grew from a relatively HREE-depleted fluid. In general, the occurrences of HREE-depleted rims in pyroxene crystals (Fig. 10) also can be attributed to the crystallization of garnets or the formation of minerals such as zircon that fractionate HREE from LREE. Two mechanisms could also be involved: changes in fluid chemical composition (*e.g.*, Dziggel et al., 2009) or simultaneous growth of other REE-bearing phases.

Trace elements and REE^{3+} are also incorporated into magnetite. Chondrite-normalized REE patterns for magnetite from the Sangan skarn are characterized by slight enrichment in LREEs relative to HREEs (Fig. 11a). However these values are significantly less than those from garnet and pyroxene cores. Huang et al. (2015) suggested that there are two generations of massive magnetites at Bayan Obo, northern China (Huang et al., 2015) including sedimentary and hydrothermal magnetite. Magnetite grains from sedimentary ores have the highest REE contents and show slight to moderate REE enrichment, whereas those from hydrothermal mag-

Table 6
Selected LA-ICP-MS analyses of magnetite from Sangan skarn.

Sample (ppm)	CNF-04	CNF-05	CNF-06	B3-07	B3-08	B3-09	Cs31-010	Cs31-011	A3-022	A3-023
Si	1363.96	2065.614	1717.343	1483.879	1437.175	1328.42	1051.798	1400.187	5207.304	2172.098
Ca	66.18346	121.5717	342.1613	58.01118	21.71526	51.60334	68.14866	117.1743	529.2728	115.2473
Sc	0.045189	0.067784	0.061821	0.124263	0.017196	0.041529	0.067685	0.052147	0.75127	0.473489
Ti	180.6818	178.3344	165.8729	2.968693	5.476670	11.49192	51.17734	48.29875	35.45489	13.28611
Fe^{3+}	243931.5	243931.5	243931.4	252196.5	252196.5	252196.5	204717.6	204717.6	245365.6	245365.6
Fe^{2+}	221124.3	221129.6	221526.9	231355.1	231258.0	231097.4	187136.1	187597.5	243344.3	244398.7
Cu	0.077512	0.150631	0.082847	0.036338	0.055156	0.079814	0.118778	0.165394	63.87688	26.49647
Rb	0.648341	0.533171	0.744368	0.276429	0.158330	0.196615	1.722416	1.677643	0.520838	0.179295
Sr	1.531414	2.049208	6.750148	0.605419	0.598281	0.815012	1.917307	2.794316	3.342835	1.275265
Y	0.027616	0.018044	0.022218	0.05149	0.008663	0.005937	0.009297	0.008875	1.167941	0.684981
Zr	0.026957	0.083161	0.235047	0.156059	0.026280	0.021965	0.061101	0.127469	0.161933	0.014205
Nb	0.045095	0.116739	0.241009	0.014373	0.025274	0.049381	0.003476	0.010482	0.048927	0.005556
Mo	0.049269	0.082847	0.103559	0.043476	0.032445	0.046072	0.057941	0.053200	3.560640	1.291048
Ba	2.535620	3.113039	6.52734	1.275078	0.899368	0.947386	3.510673	8.514632	28.82288	4.842218
La	0.054447	0.113287	0.320718	0.044157	0.030530	0.043411	0.125889	0.112194	0.435610	1.991812
Ce	0.099793	0.104186	0.275215	0.064111	0.037344	0.056292	0.181986	0.196471	0.580814	2.992453
Pr	0.009948	0.008536	0.02294	0.008273	0.002174	0.005159	0.018778	0.022439	0.074180	0.328286
Nd	0.046758	0.034833	0.065587	0.048343	0.017390	0.021024	0.069792	0.086648	0.318816	1.376276
Sm	0.016318	0.011925	0.009414	0.013951	0.007592	0.008144	0.009481	0.013168	0.111112	0.321973
Eu	0.003483	0.00317	0.002887	0.003082	0.003147	0.003082	0.001870	0.002344	0.059028	0.122476
Gd	0.016946	0.011611	0.012553	0.012329	0.007592	0.005743	0.008691	0.010271	0.171403	0.266732
Tb	0.002354	0.001444	0.001789	0.003439	0.001687	0.002823	0.001106	0.001370	0.029988	0.037248
Dy	0.007343	0.00728	0.006904	0.016449	0.006262	0.005872	0.005926	0.005320	0.208020	0.160355
Ho	0.002259	0.001883	0.002008	0.001947	0.001622	0.001200	0.001528	0.002002	0.048927	0.024180
Er	0.00477	0.008191	0.004864	0.007495	0.003796	0.003666	0.003424	0.003608	0.115216	0.043877
Tm	0.001349	0.002354	0.001506	0.001428	0.001752	0.001395	0.001264	0.001238	0.013131	0.006692
Yb	0.008253	0.009414	0.010419	0.006619	0.007981	0.006976	0.005320	0.004346	0.079231	0.041036
Lu	0.00204	0.002416	0.001695	0.001914	0.001784	0.001038	0.001185	0.001422	0.008807	0.005082
Hf	0.004174	0.006025	0.005649	0.005321	0.005159	0.004477	0.009587	0.005847	0.007955	0.009628
Ta	0.009163	0.019519	0.033296	0.002109	0.001298	0.001525	0.002370	0.001817	0.003472	0.002904
W	0.057114	0.063704	0.071863	0.160277	0.672904	2.209486	0.031867	0.042402	6.234277	0.344069
^{204}Pb	1.176804	1.032449	1.045002	1.031742	0.425026	0.279025	0.526733	0.695287	0.830185	0.688138
^{206}Pb	0.785477	1.248981	0.828784	1.301034	0.295896	0.318283	0.729525	0.658679	1.262638	1.010111
^{207}Pb	0.711417	1.154837	0.803365	1.135566	0.259558	0.334505	0.647618	0.622071	1.208976	0.918569
^{208}Pb	0.677525	1.208185	0.810896	1.262100	0.272211	0.320878	0.589150	0.627602	1.234229	0.972232
Th	0.023285	0.006057	0.020618	0.050776	0.003666	0.009604	0.006610	0.009165	0.051768	0.147097
U	0.015879	0.026863	0.009822	0.018266	0.010123	0.012589	0.057045	0.059916	1.619334	0.467176

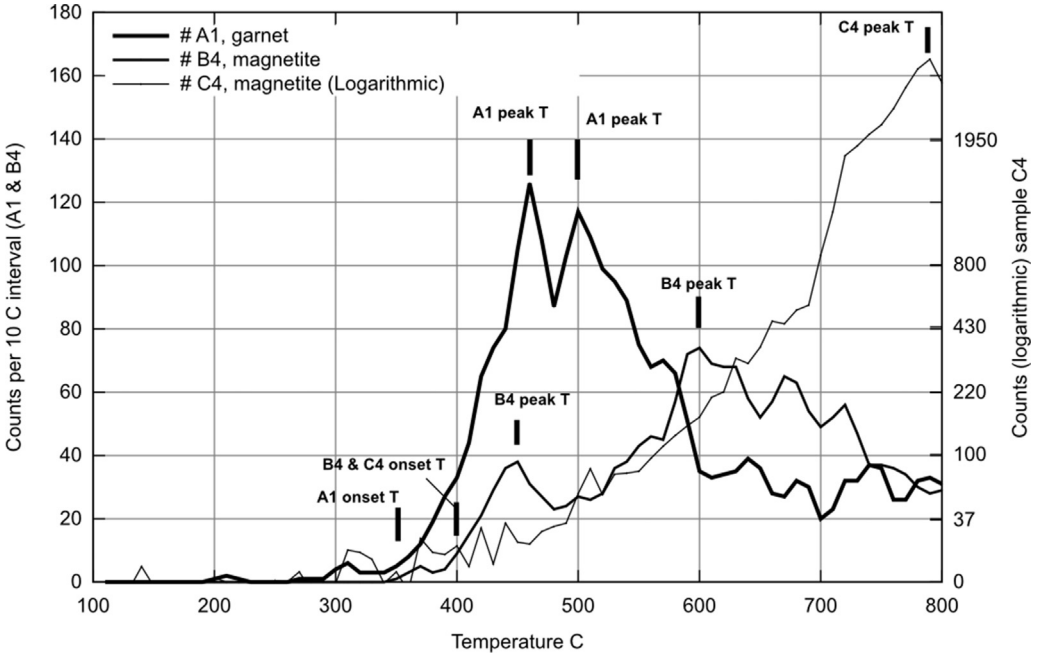

Fig. 12. Results of the baro-acoustic decrepitation of fluid inclusions hosted by minerals comprising high grade massive magnetite ores (B-4 and C-4) (magnetite dominant stage) from B and C orebodies and garnet (A-1) (silicate dominant stage) from A orebody.

netite show light REE enrichment. The REE patterns of magnetite from Sangan are quite similar to those from hydrothermal magnetite at Bayan Obo, northern China (Huang et al., 2015), indicating a similar origin. The mineral chemistry of magnetite deposited from hydrothermal fluids is mostly controlled by: (1) fluid composition, (2) temperature, (3) pressure, (4) cooling rate, (5) oxygen or sul-

fur fugacity, (6) silica activity (Nadoll et al., 2014; and references therein) and (7) composition of host rocks (Nadoll, 2010). Several of them have evidently controlled the magnetite formation in different portions of the Sangan deposits. Low abundances of Al_2O_3, TiO_2 and MgO in magnetite from Sangan indicate exsolution of ilmenite and spinel could not have occurred. The MgO content of magnetite varies as follow: 0.01–0.26 wt.% in sample A-3; up to 0.03 wt.% in sample B-2, and 0.02–0.26 in sample Cn-1. The relatively high MgO in A and Cn orebodies is consistent with their formation at relatively high temperatures (Nadoll et al., 2012). Magnetites also contain moderate to high SiO_2 (0.06–3.43 wt.% for A, B, and Cn), low MnO (0.01–0.12 wt.%, for A, B, and Cn) and low to moderate Al_2O_3 (0.05–0.43 wt.% for A, B, and Cn) contents (Table 3). Magnetite contains submicrometer-to-micrometer inclusions of quartz which indicates the oxide precipitate was chemically impure and shows high Si content in some samples in Sangan. Magnetite in the Cs orebody has low MgO (0.03–0.07 wt.%), low SiO_2 (<0.024 wt.%) and MnO (0.09–0.13) which is consistent with calcic skarns. In contrast, the range of the Cu contents of magnetite from A orebody is significantly higher than those from B, Cn and Cs. This is attributed to difference of coexisting sulfides content in all orebodies of the Sangan deposit. Titanium and V are a powerful tool to monitor for reduction-oxidation conditions and the influence of mafic materials on magnetite formation. Ti has only $Ti^{(IV)}$ in hydrothermal fluids and hence the partition coefficient is rather consistent between magnetite and fluids. The Ti/V ratio of magnetite from the western and eastern parts of the Tieshan deposit, China, ranges from 1.32 to 5.24, and 1.31 to 10.34, respectively, indicating a relatively reduced depositional environment in the western ore body (Wang et al., 2017). The Ti/V (2.00–26.0 with 12/4 **+2** as an average) ratio of magnetite from the Cn orebody is higher than those from A (2.0–11.0 with 5.7 **+2** as an average), B (2.0–11.0 with 2.9 **+2** as an average) and Cs (0.25–5.00 with 1.7 **+0.2** as an average), that indicate a relatively oxidized depositional environment for Cn orebody comapred to the other orebodies in the Sangan region.

6.2. Implications for skarn hydrothermal fluid evolution

Previous studies show that $\delta^{18}O$ values for water in isotopic equilibrium with garnet and magnetite from the Sangan area range from +7.7 to +11.6‰ and +9.8 to +14.2‰, respectively (Mazaheri, 1996), which are higher than those of magmatic water (+5.5 to +10‰: Hoefs, 2009). (Rose et al. (1985)) measured the oxygen isotope composition of magnetite from southeastern Pennsylvania ($\delta^{18}O$ = +5.2 to +10.0‰) and suggested that ^{18}O enrichment of water in equilibrium with magnetite ($\delta^{18}O_{H2O}$ = +12.3 to +17.4‰; Fig. 10a) was the result of a high temperature reaction between magmatic fluid and carbonate country rocks enriched in ^{18}O. It is thus likely that the $\delta^{18}O$ compositions of hydrothermal fluids responsible for crystallization of garnet and magnetite in the Sangan skarn increased due to interaction of magmatic water with carbonate country rocks. The minerals from the calc-silicate stage have major roles in governing REE fractionation patterns at Sangan and can thus map the evolution of the mineralizing system. Garnet compositions change from And_{35} to And_{65} in the core and And_{50} to And_{70} in the rim which suggests reducing conditions. Based on LA-ICP-MS analyses of zoned garnets, HREE-rich patterns of the core and rim indicate that garnet crystallized from a relatively HREE-rich fluid. Previous studies show that LREE chloride complexes are more stable at higher temperature whereas HREE chloride complexes are more stable at low temperatures (Williams-Jones and Heinrich, 2005). This can change partitioning of the REE between the fluid and garnet. Bau (1991) suggested that The Eu^{3+}/Eu^{2+} redox potential in hydrothermal fluids primarily depends on temperature and less on pH and pressure. However, at temperatures above 250 °C, Eu^{2+} should predominate in hydrothermal solutions (Sverjensky, 1984). Therefore, at relatively high temperatures observed in skarn systems, Eu can fractionate from the other REEs (Bau, 1991). In nearly neutral conditions, the REE patterns of the fluid are relatively HREE-enriched and LREE-depleted (*e.g.*, Bau, 1991). If fluid-rock interaction happens under mildly acidic conditions, the REE pattern of the fluid would be controlled by sorption processes and provide Eu as Eu^{2+} to a positive Eu anomaly in the fluid. The REE patterns in the zoned garnets in the Sangan skarn deposit are consistent with those patterns mentioned above (Fig. 8), suggesting they formed in near neutral to mildly acidic conditions.

Mayanovic et al. (2007) show that in hydrothermal fluids, Cl^- is a carrier for Eu^{2+} and a poor transporter for REE^{3+}. The local positive Eu anomalies in garnet and pyroxene cores might be explained by the presence of ligands, such as Cl^-, which transfer Eu^{2+}. The existence of a Eu anomaly suggests that Eu is present in the divalent state as opposed to the trivalent state of the other REEs, and thus high temperature and reducing conditions can be inferred (Gaspar et al., 2008), which is consistent with microprobe results. In contrast, chondrite-normalized REE patterns for pyroxene rims and magnetite are characterized by LREE enrichment relative to HREEs without Eu anomalies (Figs. 10 and 11). These characteristics indicate that pyroxene rims and magnetite possibly originated from fluids which were depleted in HREE by crystallization of garnets or other minerals (Zhai et al., 2014). Europium is present as Eu^{3+} under oxidizing conditions (Gaspar et al., 2008), and this likely explains its similar behavior to other REEs in magnetite and pyroxene rims (Figs. 10 and 11).

Similar to garnet from Sangan, trends described by Zhai et al. (2014) for garnets from Zhongdian area, NW Yunnan Province, China, show that they have high HREE, Th, U, Pb and Y and low in LREE, Sr, Ba, La, and Ti (Fig. 8b). Ismail et al. (2014) suggest that REE distribution patterns in mineral assemblages, garnet, diopside and feldspar define the evolution from early skarn through the calc-silicate dominant stage to the magnetite stage. They also concluded that distinct REE patterns from different stages of hydrothermal fluid evolution are related to redox changes throughout different lithologies in the Hillside IOCG-skarn. However, Zhai et al. (2014) also show that garnet cores were formed from a fluid that was generally HREE-rich, with relatively high ΣREE, high HREE/LREE ratios and negative Eu anomalies; whereas rims crystallized from a fluid that was typically LREE-rich, with relatively low ΣREE, low HREE/LREE ratios and positive Eu anomalies. They proposed that the hydrothermal fluid evolved from near neutral pH and oxidizing conditions to acidic and reducing conditions. The chondrite-normalised REE fractionation patterns for the skarn zone at Ali Abad skarn depicted by Zamanian and Radmard (2016) are similar to those from the Sangan skarn. Zamanian and Radmard (2016) showed the highest and lowest REE-enriched patterns for skarn and ore zones, respectively. They concluded that hydrothermal fluids responsible for garnet formation were mostly of magmatic origin with high REE concenteration and for magnetite formation were of magmatic and meteoric water origin with low REE concentrations. The chondrite-normalised REE fractionation patterns for garnet depicted by Xu et al. (2016) are different from the Sangan skarns, however, garnet from Sangan shows a similar YAG-type substitution mechanism. These results confirm that variations in fluid composition and physicochemical conditions are considered as major controls on incorporation of trace elements, including REEs, into garnet rather than YAG-type substitution mechanisms. As U solubility decreases with decreasing fO_2 of the hydrothermal fluid, this would increase U incorporation into garnet (*e.g.*, Smith et al., 2004). In contrast, increasing fluid fO_2 would increase U solubility and reduce U incorporation into magnetite (Fig. 13). A similar process was involved to describe U variations in garnets from the Xieertala Fe-Zn skarn deposit, northern China (Zhai et al., 2014).

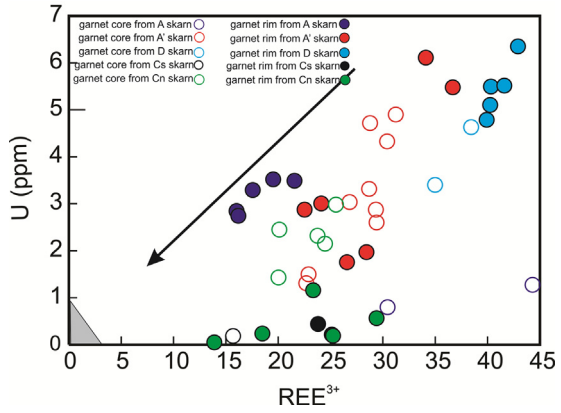

Fig. 13. Covariation of REE^{3+} with U in the Sangan garnet. Note the variations of ΣREE with U in the Sangan magnetite have been shown by grey field.

Based on the baro-acoustic decrepitation results, REE patterns and Eu anomalies in zoned garnets, pyroxene and magnetite, the hydrothermal fluid in the skarn evolved from a near neutral pH, reduced fluid with low fO_2, which was relatively HREE-rich, with positive Eu^{2+} and U-rich in the silicate-dominant stage, progressing to an acidic and oxidized fluid which was relatively HREE-depleted, with no Eu^{2+} anomaly and U-poor in the magnetite-dominant stage.

7. Conclusions

(1) *In situ* LA-ICP-MS analyses of zoned garnets, pyroxene and magnetite from Sangan skarn show that garnets were formed from a fluid that was generally HREE-rich, with relatively high ΣREE, high HREE/LREE ratios, positive Eu anomalies and U-rich characteristics whereas pyroxene rims and magnetite were crystallized from a fluid that was typically LREE-rich, withrelatively low ΣREE, low HREE/LREE ratios, with no Eu anomalies and U-poor characteristics.

(2) Analysis of REE patterns, Eu anomalies and U contents in zoned garnet, pyroxene and magnetite shows that the hydrothermal fluid in the skarn changed from a near neutral to mildly acidic pH and low fO_2 in the silicate stage towards acidic conditions and high fO_2 in the magnetite stage.

(3) The dominant substitution mechanism for REE distribution whitin the garnet is YAG-type. The results show that variations in fluid composition and physicochemical conditions rather than YAG-type substitution mechanisms are considered to have a major control on incorporating trace elements and REEs into the garnet.

(4) The calc-silicate dominant stage was progressively formed at temperatures around 350–450 °C as indicated by mineral chemistry and the decrepitation analysis of garnet. The magnetite dominant stage was progressively formed at similar or slightly higher temperature (around 400 °C) as indicated by the decrepitation analysis of magnetite. The Lack of any low-temperature peak around 300 °C indicates an absence of CO_2-rich fluid inclusions.

Acknowledgements

The authors would like to thank Professor Changqian Ma from CUG for his assistance during analyses at the GPMR. Constructive suggestions by Prof. Nigel J Cook, Dr. Cristiana Ciobanu (University of Adelaide, Australia) and Prof. Jian-Feng Gao (State Key Laboratory of Ore Deposit, China Academy of Science) substantially improved the manuscript. We would like to thank Dr. Tomas Magna for his comments and editorial handling of the paper and Dr. Jaayke Knipping and two anonymous reviewer for reviewing the manuscript and providing us with invaluable comments. This study was performed as part of a collaborative multidisciplinary research project on the Sabzevar-Doruneh magmatic belt chiefly involving the Sangan, funded by the School of Earth Resources and State Key Laboratory of Geological Processes and Mineral Resources, China University of Geosciences, Wuhan. We gratefully acknowledge the financial support from the geochemical analyses funded by Ministry of Science and Technology of China (2012CB416802).

References

Alavi Naini, M., 1982. Geological Quadrangle Map of Khaf: Series Sheet 8059, Ministry of Mines and Metals. Geological survey of Iran, Tehran.
Armbruster, T., Birrer, J., Libowitzky, E., Beran, A., 1998. Crystal chemistry of T-bearing andradites. Eur. J. Mineral. 5, 907–921.
Bau, M., 1991. Rare-earth element mobility during hydrothermal and metamorphic fluid/rock interaction and the significance of the oxidation state of Europium. Chem. Geol. 93, 219–230.
Burlinson, K., 1984. Exploration for gold at Pine Creek and Tennant Creek, N.T and at Halls Creek, W.A, using the fluid inclusion decrepitation technique. In: The Aus. I.M.M. Conference, Darwin, pp. 373–375.
Burlinson, K., 1988. An instrument for fluid inclusion decrepitometry and examples of its application. Bull. Miner. Res. Explor. 111, 3–4, 267–278.
Burlinson, K., 1990. The BGS Model 105 Decrepitometer. http://www.appliedminex.com/decrep/general/model105.htm.
Burlinson, K., 2001. Decrepitation in Haematite and Magnetite. http://appliedminex.com/decrep/general/haemag.htm.
Burlinson, K., 2012. Fluid inclusion studies on opaque minerals. ACROFI-4 Conference http://appliedminex.com/decrep/orals/bne12/opaquedecrep.htm.
Canil, D., Grondahl, C., Lacourse, T., Pisiak, L.K., 2016. Trace elements in magnetitefrom porphyry Cu-Mo-Au deposits in British Columbia, Canada. Ore Geol. Rev. 72, 1116–1128.
Chakraborty, S., Ganguly, J., 1991. Compositional zoning and cation diffusion in garnets. In: Diffusion, Atomic Ordering, and Mass Transport. Springer, US, pp. 120–175.
Chang, Z.S., Meinert, L.D., 2004. The magmatic-hydrothermal transition – evidence from quartz phenocryst textures and endoskarn abundance in Cu-Zn skarns at the Empire Mine Idaho, USA. Chem. Geol. 210, 149–171.
Cheng, H., Zhang, C., Vervoort, J.D., Lu, H.H., Wang, C., Cao, D.D., 2012. Zircon U-Pb and garnet Lu-Hf geochronology of eclogites from the Lhasa Block, Tibet. Lithos 155, 341–359.
Ciobanu, C.L., Cook, N.J., 2004. Skarn textures and a case study: the Ocna de Fier-Dognecea orefield Banat, Romania. Ore Geol. Rev. 24, 315–370.
Dare, S.A.S., Barnes, S.J., Beaudoin, G., Meric, J., Boutroy, E., Potvin-Doucet, C., 2014. Trace elements in magnetite as petrogenetic indicators. Miner. Depos. 49, 785–796.
Dupuis, C., Beaudoin, G., 2011. Discriminant diagrams for iron oxide trace element fingerprinting of mineral deposit types. Miner. Depos. 46, 319–335.
Dziggel, A., Wulff, K., Kolb, J., Meyer, F.M., Lahaye, Y., 2009. Significance of bell-shaped growth zoning in hydrothermal garnet: evidence from the Navachab gold deposit, Namibia. Chem. Geol. 262, 262–276.
Enami, M., Cong, B., Yoshida, H., Kawabe, I., 1995. A mechanism for Na incorporation in garnet: an example from garnet in orthogneiss from the Su-Lu terrane, eastern China. Am. Mineral. 80, 475–482.
Fernando, G., Hauzenberger, C.A., Baumgartner, L.P., Hofmeister, W., 2003. Modeling of magnetite dominant diffusion zoning in garnet: evidence for slow cooling of granulites from the Highland Complex of Sri Lanka. Mineral. Petrol. 78, 53–71.
Frietsch, R., Perdahl, J.A., 1995. Rare earth elements in apatite and magnetite in Kiruna type iron ores and some other iron ore types. Ore Geol. Rev. 9, 489–510.
Gaspar, M., Knaack, C., Meinert, L.D., Moretti, R., 2008. REE in skarn systems: a LA-ICP-MS study of garnets from the Crown Jewel gold deposit. Geochim. Cosmochim. Acta 72, 185–205.
Golmohammadi, A., Karimpour, M.H., Malekzadeh, A., 2015. Alteration mineralization, and radiometric ages of the source pluton at the Sangan iron skarn deposit, northeastern Iran. Ore Geol. Rev. 65, 545–563.
Grew, E.S., Marsh, J.H., Yates, M.G., Lazic, B., Armbruster, T., Locock, A., Bell, S.W., Dyar, M.D., Bernhardt, H.-J., Medenbach, O., 2010. Menzerite-(Y), a new species, $\{(Y, REE)(Ca, Fe^{2+})_2\}[(Mg, Fe^{2+})(Fe^{3+}, Al)](Si)_3O_{12}$, from a felsic granulite, Parry Sound, Ontario, and a new garnet end-member, $\{Y_2Ca\}[Mg_2](Si_3)O_{12}$. Can. Mineral. 48, 1171–1193.
Hariya, Y., Kimura, M., 1978. Optical anomaly garnet and its stabiliry field at high pressures and temperatures. J. Fac. Sci. 18, 611–624, Hokkaido University, Series IV.
Hoefs, J., 2009. Stable Isotope Geochemistry. Springer-Verlag, Berlin, Heidelberg, New York.
Hu, H., Li, J.-W., Lentz, D., Ren, Z., Zhao, X.-F., Deng, X.-D., Hall, D., 2014. Dissolution-reprecipitation process of magnetite from the Chengchao irondeposit: insights into ore genesis and implication for in-situ chemical analysisof magnetite. Ore Geol. Rev. 57, 393–405.

Huang, X., Zhou, M.-F., Qiu, Y.Z., Qi, L., 2015. In-situ LA-ICP-MS trace elemental analyses of magnetite: the Bayan Obo Fe-REE-Nb deposit, North China. Ore Geol. Rev. 65, 884–899.
Ismail, R., Ciobanu, C.L., Cook, N.J., Schmidt Mumm, A., Wade, B., Giles, D., Teale, G.S., 2014. Rare Earths and other trace elements in minerals from skarn assemblages Hillside iron oxide-copper-gold deposit, Yorke Peninsula, South Australia. Lithos 184–187, 456–477.
Jaffe, H.W., 1951. The role of yttrium and other minor elements in the garnet group. Am. Mineral. 36, 133–155.
Jamtveit, B., Wogelius, R.A., Fraser, D.G., 1993. Zonation patterns of skarn garnets: records of hydrothermal system evolution. Geology 21, 113–116.
Karimpour, M.H., 2004. Mineralogy, alteration, source rock, and tectonic setting of Iron- Oxides Cu-Au deposits and examples of Iran. In: 11th Iranian Crystallography and Mineralogy Society of Iran Conference, University of Yazad, pp. 184–189.
Kermani, A., Forster, H., 1991. Petrography, Mineralogical and geochemical investigations of the Sangan Iron ore deposit, northeastern Iran. Proceedings of Third Mining Symposium of Iran.
Kim, H.S., 2006. Deformation-induced garnet zoning. Gondwana Res. 10, 379–388.
Knipping, J.L., Bilenker, L.D., Simon, A.C., Reich, M., Barra, F., Deditius, A.P., Wälle, M., Heinrich, C.A., Holtz, F., Munizaga, R., 2015. Trace elements in magnetitefrom massive iron oxide-apatite deposits indicate a combined formation byigneous and magmatic-hydrothermal processes. Geochim. Cosmochim. Acta 171, 15–38.
Martin, L.A.J., Ballèvre, M., Boulvais, P., Halfpenny, A., Vanderhaeghe, O., Duchêne, S., Deloule, E., 2011. Garnet re-equilibration by coupled dissolution-reprecipitation: evidence from textural, major element and oxygen isotope zoning of 'cloudy' garnet. J. Metamorph. Geol. 29, 213–231.
Mazaheri, S.A., 1996. Petrological Studies of Skarns from Marulan, New South Wales, Australia and Sangan, Khorassan, Iran. University of California, Ph. D thesis, 318p.
Meinert, L.D., 1992. Skarns and skarn deposits. Geosci. Can. 19, 145–162.
Meinert, L.D., 1997. Application of skarn deposit zonation models to mineral exploration. Explor. Min. Geol. 6, 185–208.
Meinert, L.D., Nicolescu, S., 2005. World skarn deposits. In: Economic Geology 100th Anniversary Volume., pp. 299–336.
Meinert, L.D., Dipple, G.M., Nicolecu, S., 2005. World skarn deposits. In: Economic Geology 100th Anniversary Volume., pp. 299–336.
Menzer, G., 1926. Die kristallstructure von granat. Zeitschrift für Kristallographie 63, 157–158.
Mirnejad, H., Blourian, G.H., Kheikhah, M., Akrami, M.A., Tutti, F., 2008. The chemistry of hydrothermal magnetite: a review. Ore Geol. Rev. 61, 1–32.
Nadoll, P., Mauk, J.L., Hayes, T.S., Koenig, A.E., Box, S.E., 2012. Geochemistry of magnetite from hydrothermal ore deposits and host rocks of the Mesoproterozoic Belt Supergroup United States. Econ. Geol. 107, 1275–1292.
Nadoll, P., Angerer, T., Mauk, J.L., French, D., Walshe, J., 2014. The chemistry of hydrothermal magnetite: a review. Ore Geol. Rev. 61, 1–32.
Nadoll, P., 2010. Geochemistry of Magnetite from Hydrothermal Ore Deposits and Host Rocks- Case Studies from the Proterozoic Belt Supergroup, Cu-Mo-porphyry+ Skam and Climax-Mo Deposits in the Western United States. The Uiversity of Auckland, Auckland.
Nicolescu, S.Ë., Cornell, D.H., Bojar, A.V., 1999. Age and tectonic setting of BocsËa and Ocna de Fier-Dognecea granodiorites (southwest Romania) and of associated skarn mineralisation. Miner. Depos. 34, 743–753.
Ravna, E.K., 2000. The garnet-clinopyroxene Fe2+-Mg geothermometer: an updated calibration. J. Metamorph. Geol. 18, 211–219.
Rose, A.W., Herrick, D.C., Deines, P., 1985. An oxygen and sulfur isotope study of skarn-type magnetite deposits of the Cornwall type, southeastern Pennsylvania. Econ. Geol. 80, 418–443.
Russell, J.K., Dipple, G.M., Lang, J.R., Lueck, B., 1999. Major element discrimination of titanian andradites from magmatic and hydrothermal environments: an example from the Canadian Cordillera. Eur. J. Mineral. 6, 919–935.
Samadi, R., Mirnejad, H., Kawabata, H., Valizadeh, M.V., Harris, C., Gazel, E., 2014. Magmatic garnet in the Triassic (215 Ma) Dehnow pluton of NE Iran and its petrogenetic significance. Int. Geol. Rev. 5, 596–621.
Schmidt, A., Mezger, K., O'Brien, P.J., 2011. The time of eclogite formation in the ultrahigh pressure rocks of the Sulu terrane: constraints from Lu-Hf garnet geochronology. Lithos 125, 743–756.
Smith, M.P., Henderson, P., Jeffries, T.E.R., Long, J., Williams, C.T., 2004. The rare earth elements and uranium in garnets from the Beinn an Dubhaich Aureole, Skye, Scotland, UK: constraints on processes in a dynamic hydrothermal system. J. Petrol. 45, 457–484.
Sośnicka, M., Bakker, J.R., Broman, C., Pitcairn, I., Paranko, I., Burlinson, K., 2015. Fluid types and their genetic meaning for the BIF-hosted iron ores Krivoy Rog, Ukraine. Ore Geol. Rev. 68, 171–194.
Somarin, A.K., 2004. Garnet composition as an indicator of Cu mineralization: evidence from skarn deposits of NW Iran. J. Geochem. Explor. 81, 47–57.
Sun, S.S., McDonough, W.F., 1989. Chemical and isotopic systematics of oceanic basalts: implication for mantle composition and processes. In: Saunder, A.D., Norry, M.J. (Eds.), Magmatism in the Ocean Basins. Geological Society, London, pp. 313–345, Special Publications 42.
Sverjensky, D.M., 1984. Europium redox equilibria in aqueous solution. Earth and Planetary. Sci. Lett. 67, 70–78.
van Orman, J.A., Grove, T.L., Shimizu, N., 2001. Rare earth element diffusion in diopside: influence of temperature, pressure, and ionic radius and an elastic model for diffusion in silicates. Contributions to Mineralogy and Petrology 141, 687–703.
Wang, M., Wanga, W., Liu, K., Michalak, P.P., Weid, K., Hue, M., 2017. In-situ LA-ICP-MS trace elemental analyzes of magnetite: the Tieshan skarn Fe-Cu deposit, Eastern China. Chemie der Erde - Geochem. 77, 169–181.
Whitney, D.L., 1996. Garnets as open systems during regional metamorphism. Geology 24, 147–150.
Williams-Jones, A.E., Heinrich, C.A., 2005. Vapour transport of metals and the formation of magmatic-hydrothermal ore deposits. Econ. Geol. 100, 1287–1312.
Xu, J., Ciobanu, C.L., Cook, N.J., Zheng, Y., Sun, X., Wade, B.P., 2016. Skarn formation and trace elements in garnet and associated minerals from Zhibula copper deposit, Gangdese Belt, southern Tibet. Lithos 262, 213–231.
Zamanian, H., Radmard, K., 2016. Geochemistry of rare earth elements in the Baba Ali magnetite skarn deposit, western Iran – a key to determine conditions of mineralization. Geologos 22 (1), 33–47.
Zhai, D.G., Liu, J.J., Zhang, H.Y., Wang, J.P., Su, L., Yang, X.A., Wu, S.-H., 2014. Origin of oscillatory zoned garnets from the Xieertala Fe-Zn skarn deposit, northern China: in situ LA-ICP-MS evidence. Lithos 190–191, 279–291.
Zhao, W.W., Zhou, M.F., 2015. In situ LA-ICP-MS trace elemental analyses of magnetite: the Mesozoic Tengite skarn Fe deposit in the Nanling Rang, South China. Ore Geol. Rev. 65, 872–883.